SENTINEL-3 OPTICAL PRODUCTS AND ALGORITHM DEFINITION

Active Fire: Fire Detection and Fire Radiative Power Assessment

DOCUMENT REF: S3-L2-SD-03-T04-KCL-ATBD_FIREPRODUCT

DELIVERABLE REF: SD-03-T

VERSION: 4.3

CREATION DATE: 2009-07-09

LAST MODIFIED: 2019-10-31

Title: **Active Fire: Fire Detection and Fire Radiative Power**

Document Number:

Issue:4

Revision: 3

Date: 31 Oct 2019

Table of Contents

List of Figures

Acronyms and Abbreviations

AVHRR Advanced Very High Resolution Radiometer
ATBD Algorithm Theoretical Basis Document
(A)ATST (Advanced) Along track Scanning Radiometer
BT Brightness Temperature
CLM CLoud Mask
EO Earth Observation
ECV Essential Climate Variable
FRP Fire Radiative Power
FRE Fire Radiative Energy
GTOS Global Terrestrial Observing System
LUT Look-Up Table
LWIR LongWave InfraRed
MAD Mean Absolute Deviation
MIR Middle InfraRed
MWIR Mid-Wave InfraRed
MODIS Moderate-Resolution Imaging Spectroradiometer
PSF Point Spread Function
ROI Region of Interest
SLSTR Sea and Land Surface Temperature Radiometer
SWIR shortwave InfraRed
VIS Visible spectral region

The Sentinel-3 SLSTR channel naming convention and the matching scientific notation used throughout this document is detailed in Appendix A.

1 INTRODUCTION

1.1 Background

This document describes the theory for the prototype multi-channel active fire detection and fire radiative power characterisation algorithm to be based on data from the Sea and Land Surface Temperature Radiometer (SLSTR) sensor onboard the Copernicus Sentinel-3 satellite. It therefore provides a detailed description of the algorithm to be used in the production of the SLSTR Active Fire Product, which consists of both Active Fire Detection and Fire Radiative Power assessment. The algorithm was initially designed to detect and characterise vegetation fires burning on the land surface areas, whilst also identifying elevated temperature sites of active volcanism and sufficiently hot industrial heat sources, and has subsequently been adapted for the detection of offshore gas flares (i.e. detection of hotspots over the open ocean and in coastal regions and potentially large lakes). The algorithm described in this version of the ATBD is designed to work at night in all areas of the Earth, and by day in areas where the standard middle infrared band of SLSTR (S7) remains unsaturated over the ambient background (i.e. the "classical" situations normally addressed by active fire detection algorithms such as that applied to MODIS e.g. Giglio et al., 2003). Saturation is experienced by SLSTR in the S7 channel over higher temperature ambient land surfaces, and in this case a future iteration of the algorithm described here will be implemented that makes wider use of the SLSTR F1 middle infrared band to cope with such situations. Since the F1 measurements are not perfectly co-located with the S7 measurements, development of this "non-classic" case requires a further evolution of the algorithm presented herein.

In the algorithm presented here, the characterisation of vegetation fires is undertaken via a calculation of their fire radiative power (FRP) output. FRP represents a measure of the fires total radiative power output integrated over all wavelengths and over the viewing hemisphere encompassing the fire (i.e. the azimuthal angles). FRP is also calculated for other types of detected hotspots, beyond vegetation fires. For simplicity, the different classes of hotspot are here referred to primarily as "Land Hotspots" and "Ocean hotspots". In the detailed description, the word "fire" is generally used to refer to all types of hotspot potentially encountered, including vegetation fires, volcanoes and gas flares. Occasionally the word 'hotspot' is used to provide clarity when talking specifically about a specific hotspot type.

1.2 The burning of vegetation, together with surface organic matter such as carbon-rich peatland soils, occurs annually across many millions of square kilometres of the Earth surface and perturbs a greater area over a wider variety of biomes than any other natural disturbance agent (Lavorel *et al.*, 2006). The widespread nature, and sporadic, unpredictable character of fire, means that frequent data from Earth Observation (EO) satellites are key for providing information necessary for the large-scale investigation and quantification of biomass burning and its consequences, such as the resulting emissions into the atmosphere of carbon, trace gases and aerosol. The SLSTR Active Fire algorithm is designed to produce two products highlighted by the UNFCC-defined Essential Climate Variables related to 'Fire Disturbance', namely *Active Fire* [detection] and *Fire Radiative Power* [fire characterisation] (Sessa and Dolman, 2008; Csizar *at al.,* 2008). *Active Fire* records the time and location of fires that were burning as the sensor imaged the Earth surface, expressed either in spatial and temporal coordinates or by an indicator of fire presence or absence in a raster map. Active fire detections are used, for example, to identify fire emissions source locations and timings, to determine fire-related parameters within ecosystem models having a representation of fire (such as fire rate of spread), and to identify fire seasonal cycles and spatio-temporal trends, potentially in relation to environmental variations such as climate change (e.g. Levine *et al.,* 1996a, 1996b; Kaufman *et al.,* 1998; Wooster and Strub, 2002; Sukhinin *et al.,* 2004; Csiszar *et al.,* 2005; Giglio *et al.*, 2006a, Giglio *et al.*, 2006b; Lodoba and Csiszar, 2007). Fire Radiative Power (FRP) is the rate at which the actively burning fire is emitting radiative energy [at the time of observation] expressed in units of power (Js^{-1} or Watts). This radiative emission is primarily in the infrared, though fires emit visible light as well (seen for example as their luminous "flames"). Through a series of airborne, ground-based and satellite data intercomparisons, FRP has been shown to be well related to the rate of fuel consumption, smoke aerosol production, and trace gas release, and thus offers a direct route for quantifying the magnitude of these processes (Kaufman *et al.*, 1998; Wooster *et al.,* 2005; Ichoku and Kaufman, 2005; Jordan *et al.*, 2007; Freeborn *et al.,* 2008).Purpose and Scope

Open vegetation fires are critical elements in the Earth System, acting as a widespread agent of change by altering land cover properties, consuming very significant quantities of terrestrial vegetation, and releasing copious amounts of trace gases and aerosols (Lavorel *et al.,* 1996). Such fire activity acts across all vegetated continents but is often highly variable in its magnitude and specific location, making satellite EO data key in its quantification (Bond and van Wilgen, 1996). A marked seasonality is also often present in response to annual climate variability, as Figure 1 demonstrates. Data on fire activity is used within many areas of terrestrial environmental research, such as for prescribing the source terms for regional or global atmospheric emissions of carbon, trace gases and aerosols, and for developing periodic assessments of land cover changes such as tropical deforestation. The information is also used in fire and ecosystem management planning and operation (such as fire use, preparedness and wildfire suppression) and for informed policy development (Csiszar *et al.,* 2008).

Polar-orbiting imaging sensors such as the Sentinel-3 SLSTR can provide data on each of the 'Fire Disturbance' Essential Climate Variables (ECVs) identified by the Global Terrestrial Observing System (GTOS) as being necessary for determining transient change, adaptation, impact and mitigation possibilities in relation to climate and associated environmental changes, namely *Burned Area*, *Active Fire* and *Fire Radiative Power* (Sessa and Dolman, 2008). This Algorithm Theoretical Basis Document (ATBD) describes the prototype algorithm that is used to derive the *Active Fire* and *Fire Radiative Power* variables. The SLSTR spectral bands in the solar reflected and thermal emissive parts of the electromagnetic spectrum (S1 to S8, plus F1) allow it to deliver these ECVs using a consistent, standardised set of tests operating over the entire Earth, frequently and repetitively.

Individual pixels containing active fires are detected based on signal increases above the ambient background, in particular in the middle infrared wavelength region which is extremely sensitive to even highly-sub pixel high temperature objects. Signals assessed in the sensors solar reflective and longwave infrared channels are used to decrease the probability of false alarms, for example caused by sunglints from small water bodies or from solar heated warm ground. Estimates of the FRP being emitted by the high-temperature object within the identified active fire pixel are made via an assessment of the middle infrared channel signal increase over the surrounding ambient background pixels. The algorithm used is the Middle infrared (MIR) radiance FRP approach, developed by Wooster *et al.* (2003; 2005) and first applied operationally in the SEVIRI FRP product (Roberts and Wooster, 2008). The same MIR radiance FRP approach is now used in many operational fire products, including the Collection 6 MODIS Active Fire products (Giglio et al, 2016). Due to their higher temperatures, FRP retrievals over gas flares are best made using an adaptation of the approach based on SWIR (rather than MIR) -measured signals (Fisher and Wooster, 2018). The pre-launch version of the SLSTR active fire detection and FRP characterisation algorithm was presented in Wooster *et al.* (2012), focused on land-based vegetation fires only at that time. The algorithm presented here is also applicable to these, but also to gas flares and other hotspots such as volcanoes, and also works over the ocean. This version of the algorithm does not account for areas that are saturated in the standard SLSTR middle infrared band (S7), and this "non-classical" situation (i.e. that does not occur with sensors such as MODIS and SEVIRI) will be dealt with via a future algorithm update.

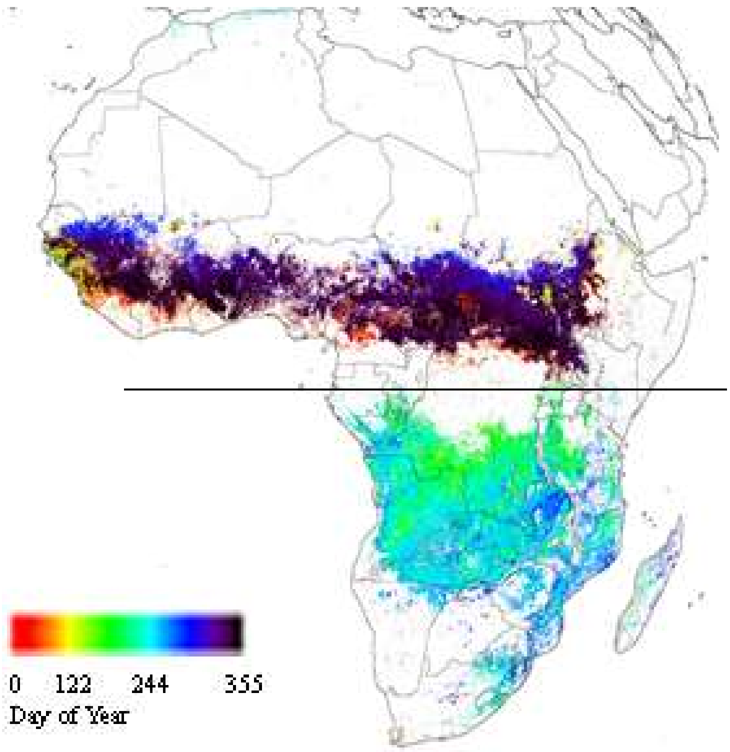

Figure 1. Fire location and timing recorded across Africa by Meteosat SEVIRI. The SEVIRI Fire Radiative Power product is delivered by the Land Satellite Applications Facility (Roberts and Wooster, 2008; http://landsaf.meteo.pt/). The marked seasonality follows the dry seasons in north and southern Africa. The equator separating northern and southern hemisphere Africa is also indicated.

Geostationary EO satellites provide the highest temporal resolution active fire data. The EUMETSAT Land Surface Analysis Satellite Applications Facility (http://landsaf.meteo.pt/) provides near real-time active fire and FRP data for Africa, Europe and parts of South America from the Meteosat Second Generation series of geostationary satellites (Figure 1). These data can be used to demonstrate the marked fire diurnal cycle seen in many environments (Figure 2), and indicate the necessity to detect fires by daytime when they are most active – not just during the night time when detection is typically somewhat easier due to the cooler background and lack of incoming solar radiation. Though geostationary data having pixel sizes 2 km to 4 km are extremely useful for the active fire application (e.g. Wooster et al., 2015), they are limited in their ability to detect and characterise the smaller and/or less intensely burning component of the active fire regime, due to their coarse spatial resolution, yet these types of fire are more common than the largest, highest intensity events. Since assessment of the full extent of fire activity is central to providing accurate and reliable data for environmental science and policy development, active fire observations from higher spatial resolution polar orbiting sensors such as SLSTR remain essential. Furthermore, not all current geostationary sensors possess the IR channel sensor characteristics necessary to detect and characterise active fires, so large gaps remain in the global record, and the view from geostationary orbit offers poor coverage of key fire-affected areas at higher latitudes (i.e. the boreal zone). The SLSTR Active Fire Product will therefore provide important data to support the generation of a long-term, global-scale 'Fire Disturbance' ECV record that will enable further characterisation of Earth's fire regimes. The version of the algorithm described here is also designed with the potential to detect offshore gas flares (i.e. detection of hotspots over the open ocean and in coastal regions) due to interest in monitoring the spatial extent and quantitative trends of such industrial combustion activity. As already stated however, it will not operate in land areas where the S7 channel of SLSTR is saturated over the ambient background. A future algorithm evolution will cope with this situation.

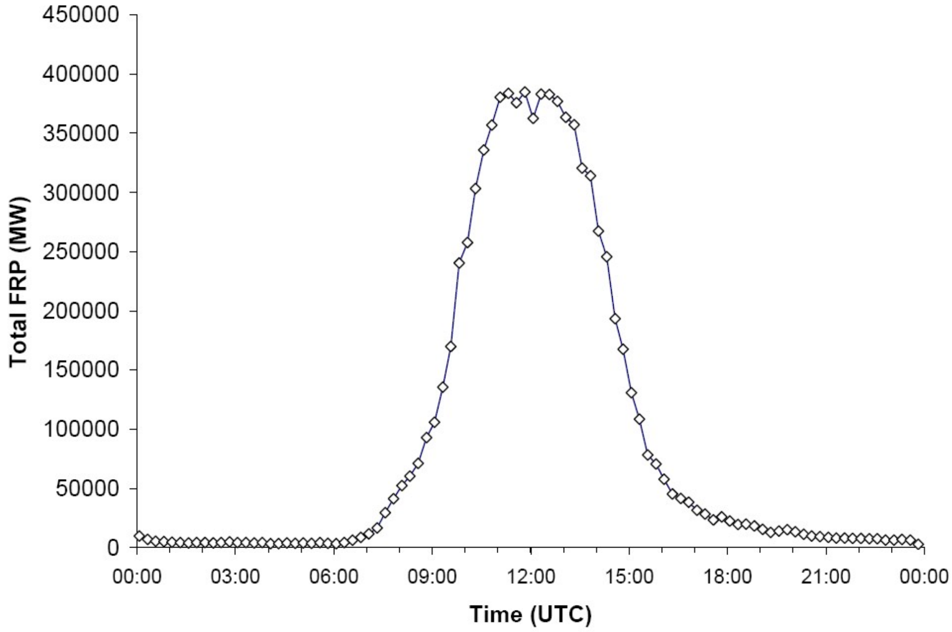

Figure 2. Diurnal cycle of total fire radiative power recorded by the Meteosat SEVIRI FRP product across southern Africa. The FRP data was recorded every 15 minutes on 14 July 2004. Local time across the region is up to three hours in advance of UTC. A very strong fire diurnal cycle is clearly evident. At the peak, around 5000 active fire pixels were detected across southern Africa (see Fig. 1), producing a combined FRP of 382 GW. When adjusted for the effects of cloud cover, atmospheric absorption and the presence of undetected smaller/low intensity fires this suggests that at least 250 tonnes of vegetation per second was being burned in order to generate this rate of radiant energy release (Wooster *et al.*, 2005).

Table 1. SENTINEL-3 SLSTR channel naming convention. Note that the F1 and F2 'fire channels' have greatly increased saturation temperatures compared to the matching standard ('S') IR channels operating at the same wavelengths (S7 and S8), though at the expense of increased noise characteristics. Currently it is expected that the S7 channel starts to saturate at values exceeding 311 K.

SLSTR Channel Name	Used for Spectral Radiance (L) and/or Brightness Temperature (T) and or Spectral Reflectance (ρ) Measure in ATBD	Central Wavelength (µm)	Waveband Width (µm)	Spatial Sampling Distance (Nadir Swath / km)
S1	-	0.555	0.02	0.5
S2	L_{RED} and ρ_{RED}	0.659	0.02	0.5
S3	ρ_{NIR}	0.865	0.02	0.5
S4	-	1.375	0.015	0.5
S5		1.61	0.06	0.5
S6	L_{SWIR2} and ρ_{SWIR2}	2.25	0.05	0.5
S7	L_{TIR} and T_{TIR}	3.74	0.38	1.0
S8	L_{TIR} and T_{TIR}	10.95	0.9	1.0
S9	T_{TIR2}	12	1.0	1.0
F1	L_{MIR} and T_{MIR}	3.74	0.38	1.0
F2	L_{TIR} and T_{TIR}	10.95	0.9	1.0

Note that whilst the SLSTR active fire (AF) detection and fire radiative power (FRP) retrieval algorithm uses data from many of the SLSTR spectral channels, it is mainly reliant on data from the MIR 3.7 µm channel (bands S7 and F1) and thermal infrared (TIR) 10.8 µm channel (bands S8 and F2,Table 1). The precision of the measurements of the BT in normal range (from 273 to $S7_{AT}$ = 311 K when S7 become nonlinear) in the 'standard' MIR and TIR bands (S7 and S8 respectively) is considerably better than that in the dedicated 'fire' channels (F1 and F2). However, non-linearity of the S7 band has been noted above a recorded BT of around 311 K ($S7_{AT}$) and full saturation of the channel at a reported brightness temperature of around 312 K, significantly lower than 323 K originally specified. This makes S7 quite commonly saturated over hotter ambient land surfaces, and very often saturated over active fires, and F1 is therefore required to be used in the AF detection and FRP retrieval process more commonly than expected pre-launch. Since the F1 detectors are not co-incident on the focal plane with the 'S' band detectors, the pixels of this channel have a different ground FOV and orientation compared to S7 (Wooster et al., 2012).

Warmer land areas will certainly have many pixels saturated in S7, and this effectively hinders detection of active fires in such locations since the presence of fire cannot increase T_{S7} any further. This will affect many daytime scenes, but is not expected to impact many nighttime scenes. To define those scenes which have significant ambient background saturation in S7, the number of pixels in the sub-scene being analysed having an $T_{S7} > S7_{AT}$ is recorded. This number is compared to the total number of cloud free land pixels in the sub-scene and if their fraction exceeds a pre-set empirical threshold (currently set as 0.01[1%] through testing of a series of SLST scenes), the subscene will be considered to have too many background pixels having BT > $S7_{AT}$. A sub-scene is extremely unlikely to have enough active fire pixels to cause this threshold to be exceeded, and so this threshold considered a simple but effective method of identifying sub-scenes containing many saturated S7 pixels that are simply too warm to be recorded without saturation in the S7 channel.

We define sub-scenes exceeding this 1% criteria as "daytime background saturation scenes" and they are not used further for the contextual AF detection process, though detection of active fire pixels with the absolute threshold test does still proceed with these subscenes. A separate algorithm to undertake a full range of active fire detection and FRP retrieval will be designed for these scenes.

Those daytime sub-scenes having less than 1% of pixels with $T_{S7} > S7_{AT}$ we define as "classic" daytime scenes and the AF fire detection and FRP retrieval process proceeds using the method outlined herein, as it does on the nighttime scenes (almost all of which are expected to meet this criteria).

1.3 Algorithm Identification

When observed from space with moderate spatial resolution instruments (~ km scale pixels such as those of SLSTR), actively burning fires represent sub-pixel features; typically covering only a very small fraction of the individual detector ground field of view. Optimum active fire detection in such circumstances generally requires that the sensor possesses spectral channels in the middle-infrared (MIR; 3-5 µm) and thermal-infrared (TIR; 8-12µm) regions. Data from solar reflective (VIS) channels are used to assist with false alarm identification, for example by removing pixels affected by sunglint whose strong MIR signals can look very similar to those of fire pixels. Potential fire pixels can be identified via multi-channel thresholding of the TIR, MIR and VIS band data, but if the algorithm is to remain effective over large areas, as well as through seasonal cycles, the specific thresholds used must be allowed to vary with environmental condition (Flasse and Ceccato, 1996). For this reason, a self-adaptive, contextual fire detection scheme whose thresholds vary in response to the background signals recorded at confirmed non-fire pixels has been identified as the most effective approach for use with SLSTR.

One advantage of SLSTR for this application, compared to some other moderate spatial resolution sensors, is that its two SWIR bands including S5 and S6 (1.6 and 2.2 µm) continue to operate at night. Elevated temperature targets emit thermal radiation in these wavebands, and since there is no solar reflected radiation at night, only such hotspots show a strong SWIR signal. This facilitates their detection further compared to use of the MIR and TIR bands alone. Casadio *et al.* (2012) used absolute thresholding tests to detect gas flare locations with night-time 1.6 μm band SWIR data from The Along Track Scanning Radiometer (ATSR), and Wooster and Rothery (1997) had previously done so with volcanoes, and similar tests are employed here to detect gas flares at night with SLSTR (as well as vegetation fires and volcanoes), though based on the 2.2 μm since the contrast with the background is highest in this SWIR band.

Once detected, the FRP can be estimated from the fire pixel signal increases measured in the sensors thermal channel(s). Generally this is assessed with respect to the neighbouring ambient background signal. One candidate for a method to estimate the FRP is simply the Stefan-Boltzmann Law, but this requires the instantaneous fire effective temperature (T_f) and sub-pixel fractional area (p_f) [since the fires are not resolved at the scale of SLSTR pixels]. These parameters can be determined using the so-called bi-spectral approach, based on simultaneous TIR and MIR channel radiance measurements made at the fire pixel and at the surrounding non-fire pixels, and this method has been used to retrieve FRP from data collected by the Bi-Spectral Infrared Detection (BIRD) Hot-Spot Recognition System (HSRS) Satellite, as well as from various other spaceborne and airborne sensors (Zhukov *et al.,* 2006). However, fire signals in the TIR channel are much weaker than in the MIR channel, yet the bi-spectral approach requires that both be well characterised for optimum retrieval accuracy. As a result, bi-spectral retrievals can be subject to large errors when variability in the TIR brightness temperatures of the non-fire background pixels means that the degree to which the fire pixel TIR channel signal is raised above the TIR background signal cannot be precisely determined (Giglio and Kendall, 2001; Wooster *et al.,* 2003). This effect will typically be much more significant for the kilometre scale SLSTR pixels than for the BIRD HSRS pixels that were 10x smaller in area, since a particular fire will represent a smaller proportional area in a larger pixel and will thus increase the fire pixel signal by a lesser amount. In addition, Shephard and Kennelly (2003) indicate the significant impact that band-to-band co-registration errors have on fire characterisation retrievals made with the bi-spectral method. They demonstrate that for a 1-km horizontal spatial resolution pixel, a 10% inter-channel co-registration error generates retrieval errors of the order of 150 K and 210 % for the effective fire temperature and fractional fire area terms respectively. In the BIRD HSRS processing chain, this effect was dealt with by clustering spatially contiguous fire pixels, and analysing the mean MIR and TIR signals recorded at the cluster scale to estimate the instantaneous cluster effective temperature (T_f) and sub-pixel area (A_f), rather than deriving per-pixel measures (Zhukov *et al.,* 2006). In this way the sensitivity to band-to-band co-registration errors was reduced considerably.

However, because of the constraints of the bi-spectral approach, especially when applied to coarser scale remote sensing data, the MODIS Collection 5 fire products used a non-linear, empirical relationship between FRP and the fire pixel MIR brightness temperature increase above the background to derive FRP (Kaufman *et al.,* 1998, Giglio *et al.*, 2003). This relationship was itself derived using multiple simulations of MODIS observations of sub-pixel sized fires (Kaufman *et al.*, 1998). By using only a single waveband, the effect of inter-channel co-registration errors is removed, and by using the MIR waveband where the fire signal is strongest the errors induced due to uncertainty in the ambient background signal are minimised.

A new algorithm for FRP estimation was derived by Wooster *et al.* (2003), by approximating the Planck Function at MIR wavelengths by a power law valid over the range of temperatures seen in open vegetation fires. In this so-called 'MIR radiance method', FRP is linearly related to the fire pixel MIR radiance increase above the surrounding non-fire background. Wooster *et al.* (2003) used BIRD data to show that the MIR radiance method produced FRP estimates that agreed well with those from the bi-spectral method, as long as fire temperatures exceed ~ 650 K, which is generally the case for all but the most weakly smouldering events. Wooster *et al.* (2003) also demonstrated the approach to be capable of producing reliable FRP retrievals in cases where the bi-spectral approach was severely affected by large variability in the brightness temperatures of the ambient background. The MIR radiance method has been adopted for use with the Meteosat FRP Pixel product produced operationally at the EUMTESAT LandSAF (Roberts and Wooster, 2008) and will be the approach used here for characterisation of active fire data from SLSTR. From Collection 6, the MODIS active fire products have also used the MIR radiance approach for FRP retrieval (Giglio *et al.*, 2016).

Gas flares typically have emitter temperatures >1500 K, significantly higher than those of vegetation fires, and Wien's Displacement law shows their maximum spectral radiant emittance is well within the SWIR band. Thus their FRP is best retrieved using SWIR band signals rather than those in the MIR (Fisher and Wooster, 2018), and this technique is employed herein.

1.4 Algorithm Heritage

Though it was designed with the key purpose of providing long-term, highly accurate observations of sea surface temperature (SST), the (A)ATSR series of sensors that are the heritage instruments for SLSTR do possess the MIR and TIR spectral channels necessary for fire detection, though their relatively low dynamic range (optimised for cloud and SST measurements) meant that daytime saturation of the MIR channel over warm terrestrial surfaces restricted routine active fire detection to night time only. Nevertheless, the resulting ATSR World Fire Atlas (WFA) is currently the longest available global active fire dataset (Orino *et al.,* 2007) and have been used to support databases representing the global fire emissions record (e.g. Van der Werf *et al.,* 2006) as well as a wide range of science studies (e.g. Thompson *et al.,*2001; Schultz, 2002; Generoso *et al.,* 2003; Sinha *et al.*, 2004), including volcanoes (e.g. Wooster and Rothery, 1997) and gas flares (Casadio *et al.*, 2012).

The simple 'fixed threshold' active fire detection approach used within the WFA is far from optimum when considering the algorithmic possibilities for use with the SLSTR fire product, which is required to operate under a wide range of environmental conditions by day as well as by night. Daytime thermal conditions vary much more markedly between areas and over time than do night time conditions, and a contextual approach with self-adapting detection thresholds is required for optimum fire detection performance and false alarm minimisation. The MODIS fire detection algorithm (Giglio *et al.,* 2003) works on these principles, as does the Bi-Spectral Infrared Detection (BIRD) Hot Spot Recognition Sensor (HSRS) fire detection scheme (Zhukov *et al.,* 2006) and the geostationary fire detection algorithm of Roberts and Wooster (2008). The SLSTR fire detection algorithm is therefore based on this contextual, self-adapting approach, using and blending many of the tests originally formulated in these pervious schemes but with adjustments for the specific spectral coverage provided by SLSTR and with new additions to take into account the detection of offshore gas flares in addition to land-based hotspots. Perhaps the most significant adjustment with respect to fire is the absence of a 3.9 µm channel on SLSTR, which necessities the use of the shorter wavelength 3.7 µm MIR spectral band (S7 and F1) instead, and the fact that measurements from the 500 m spatial resolution SWIR bands (S5 and S6) are available to aid land hotspot detection at night (and ocean hotspot detection by day). The well-tested MODIS fire detection algorithm of Giglio *et al.* (2003) is the basis for the majority of the detection tests applied here, since in terms of data for deriving active fire products MODIS is the currently operating sensor that most closely matches SLSTR. However, in order to attempt to maximise performance, the method for detection of a potential fire pixels has been adjusted to become less conservative that that used in the MODIS algorithm, whilst the spatial filter from the geostationary algorithm of Roberts and Wooster (2008) is used to constrain the number of potential fire pixels passed to the next algorithm stage. The coefficients of this spatial filter are taken from image blocks rather than the entire image, in a manner akin to the first stage of the BIRD HSRS algorithm (Zhukov *et al.,* 2006). Certain specific additions in relation to gas flare detection were informed by the work of Gallegos *et al.* (2007), and following hotspot detection, characterisation is conducted using the

MIR radiance method of FRP retrieval (Wooster *et al.*, 2003), though with parallel implementation of the SWIR radiance method which is more appropriate for gas flares (Fisher and Wooster, 2018). The pre-launch version of the SLSTR active fire detection and FRP characterisation algorithm was presented in Wooster *et al.* (2012), focused on land-based active fires only at that time. Since the mis registration between the two MIR channels F1 and S7, a cluster based algorithm have been introduced to match the same fire cluster between the two channels.

2 ALGORITHM OVERVIEW – PHYSICS OF THE PROBLEM

2.1 Background

Vegetation fires exhibit a wide temperature range, generated by activity from smouldering to intense flaming combustion, but flame radiometric temperatures of ~ 750 - 1200 K appear dominant (Sullivan *et al.,* 2003), whilst gas flares can reach significantly higher temperatures (> 1500 K). Wien's Displacement Law indicates that the peak of thermal emission from such fires occurs in or close to the shortwave Infrared (SWIR; 1.6 – 2.5 µm) or Middle Infrared (MIR; 3 – 5 µm) atmospheric windows, depending upon the combustion temperature. Fires are typically very much more active by day than by night (Figure 2), but by day the presence of potentially strong solar reflective signals in the SWIR means that the detection of active fires based on SWIR signals seen in moderate spatial resolution EO data can be difficult and prone to error. Generally day time active fire detection algorithms are therefore mostly focused on exploitation of the MIR signal, where the emission from the fire is still very strong yet where solar reflected radiation signals are far weaker than in the SWIR (Robinson, 1991). The MIR region is therefore the spectral region where active fires usually show their greatest contrast with their surrounding background pixels. In fact, parameterisation of the Planck function with the temperatures indicative of open vegetation fires indicates that in the MIR spectral region the spectral emission from an open vegetation fire can be up to four orders of magnitude greater than that from the ambient temperature background (Figure 3). Since the SLSTR has a MIR band centered on 3.7 µm, this band is the most suitable for use as the basis for active fire detection, whilst the SWIR bands can also contribute significantly at night.

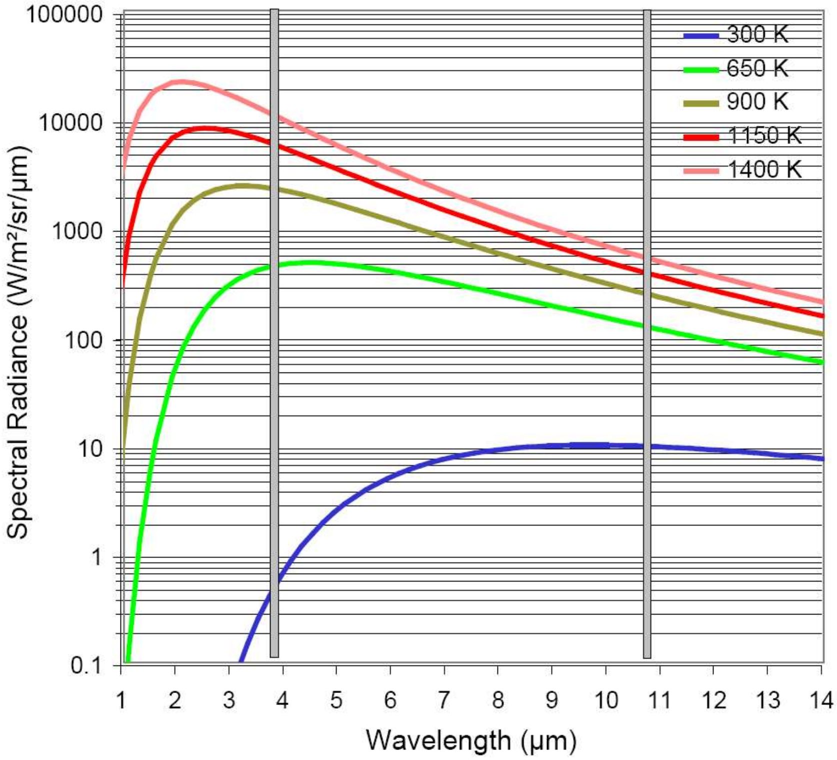

Figure 3. Spectral radiance emitted from blackbodies. The Earth ambient temperature is 300 K and the vegetation fire have a range temperatures from 650 to 1400 K. The approximate central wavelengths of the SLSTR MIR (3.7 µm) and TIR1 (10.8 µm) channel are also indicated. As temperature increases the spectral radiance increases more rapidly at MIR wavelengths than at TIR wavelengths. Note the logarithmic y-axis scale.

The intense MIR thermal signals from combusting biomass and other heat sources of similar temperature means that pixels containing actively burning fires or other sub-pixel hot targets can be discriminated via their significant increase in MIR pixel radiance or brightness temperature, even if the hot area covers only $10^{-3} – 10^{-4}$ of the pixel planimetric area (Robinson, 1991). This makes active fire detection possible using even rather coarse spatial resolution data (e.g. from geostationary systems), or even from spatially-averaged Earth observation data such as AVHRR GAC imagery (e.g. Wooster and Strub, 2002). Fire pixels generally show elevated signals in the MIR region, as already described (Robinson, 2001), and so active fire detection algorithms are generally based on identification of an increased MIR channel signal and/or by a divergent MIR and TIR brightness temperature signal. Other tests are usually added to optimize sensitivity to fires whilst minimizing false alarms. FRP characterisation in addition requires that the spectral channels used (especially the MIR channel) have a wide enough dynamic range such that they do not saturate at active fire pixels. Under certain circumstances, observations in the SLSTR SWIR bands (S5 and S6; operating at 1.6 and 2.2 microns respectively as detailed in Table 1) can also be used to aid hotspot detection since as Figure 3 demonstrates objects at many hundreds of Kelvin above ambient temperatures emit significant amounts of infrared radiation at these wavelengths, albeit by day over the land surface these signals are usually eclipsed in magnitude by reflected solar radiation. S6 is slightly better than S5 as S5 is optimal for high temperature gas glare detection and characterization, however, S6 is can detect both vegetable fires and gas flares, therefore we only use S6 for fire detection and FRP retrieval.

Care must be taken when designing hotspot detection algorithms however, since by day solar-heating on bare ground and specularly reflected sunlight can also increase MIR pixel signals far above those of surrounding areas, and thus especially by day active fire detection algorithms must use a series of additional multi-spectral optical and thermal channel tests to discriminate true fire pixels from such "false alarms". Pixels that are homogeneously hot due to solar heating of, for example, bare rock or soil surfaces should have similar MIR and TIR brightness temperatures (albeit somewhat different due to differing atmospheric and surface emissivity and solar reflection effects). Pixels containing sub-pixel sized fires can have large MIR and TIR brightness temperature differences. Pixels that show a high MIR signal due to sunglint from (potentially sub-pixel sized) water bodies also show a markedly increased VIS channel signal, but pixels containing sub-pixel fires typically do not. Using such multispectral properties, true fire pixels can be discriminated from false alarms.

Such false alarm discrimination is particularly required during use of daytime active fire detection methods, and daytime data is required since using only nighttime data will markedly underestimate fire activity (Figure 2). Once an active fire pixel is detected, the radiative power of the fires present within it can be determined from the signal increase induced by the fire compared to if the fire were not present. This requires unsaturated observations to be available in the sensors thermal channels, and thus generally necessitates a sensor with an extended dynamic range (e.g. extending to 450 to 500 K in the case of 1 km sensors such as MODIS and SLSTR). The exact saturation temperature required is typically inversely related to the size of the pixels ground field of view, as a fire will contribute proportionally less of the pixel's area weighted average signal as the pixel increases in area. In the most extreme case, a very high spatial resolution sensor (e.g. 10 m pixels) would allow the fire to be full resolved and thus the dynamic range would need to extend to ~ 1300 K. This is not the case for the moderate spatial resolution SLSTR sensor, where the fires will very likely only cover a relatively small proportion of the 1km nadir view pixel area (and a typically smaller proportion away from nadir).

2.2 Active Fire Detection Principles

Consider a pixels ground field of view of uniform background temperature T_b, containing a sub-pixel fire of effective radiant temperature T_f and effective fractional area P_f. Assuming a unitary emissivity and neglecting atmospheric and solar reflected radiation effects for the present case, the observed spectral radiance (L_λ) in two different spectral bands that can be approximated by central wavelengths in the MIR and TIR regions can be simply assumed to be the area weighted sum of that from the two individual thermal components (Dozier, 1981; Giglio and Justice, 2003).

$$L_{MIR} = p_f B(\lambda_{MIR}, T_f) + (1 - p_f) B(\lambda_{MIR}, T_b) \qquad (1)$$

$$L_{TIR} = p_f B(\lambda_{TIR}, T_f) + (1 - p_f) B(\lambda_{TIR}, T_b) \qquad (2)$$

Where $B(\lambda, T)$ is the Planck function at wavelength λ and temperature T.

Given the Planck function relationships shown in Figure 3, the presence of a subpixel sized fire within the ground FOV will enhance the pixel integrated spectral radiance (L_λ) much more in the MIR than in the TIR. Converting L_{MIR} and L_{TIR} into the equivalent brightness temperatures T_{MIR} and T_{TIR} through the inverse Planck function therefore results in $T_{MIR} >> T_{TIR}$. The magnitude of this T_{MIR} - T_{TIR} brightness temperature difference (which we here term $\Delta T_{MIR\text{-}TIR}$) increases with increasing T_f and p_f, up to the point where the fire starts to cover a very large proportion [>10%] of the pixel (Figure 4). A > 10% coverage by fire will be a very rare (potentially non-existent) occurrence for a moderate spatial resolution sensor such as SLSTR. Active fire detection algorithms are therefore generally based on thresholding pixel level observations of T_{MIR} and $\Delta T_{MIR\text{-}TIR}$ to discriminate fire pixels from non-fire pixels. Thresholds must be carefully chosen, since even certain non-fire pixels can have substantially increased values of T_{MIR} and $\Delta T_{MIR\text{-}TIR}$ due, for example, to intense solar heating or where atmospheric and surface emissivity effects are large. An approach using fixed spatially and/or temporally thresholds is therefore not effective for an algorithm required to be applied globally across all regions and seasons and by day and by night, so a contextual approach is adopted whereby fire pixels are identified based on their signal contrast with the surrounding non-fire ambient 'background' pixels (Flasse and Ceccato, 1996). Strong contrast with the background in terms of the T_{MIR} and $\Delta T_{MIR\text{-}TIR}$ measures is the basic detection criteria, with additional multi-spectral tests using both TIR and VIS channels aimed at preventing false alarms from, for example, uniformly warm surfaces and reflected sunglint (Giglio et al., 2003; Wooster et al., 2012). The details of these tests as applied to SLSTR are described in full in Section 3.

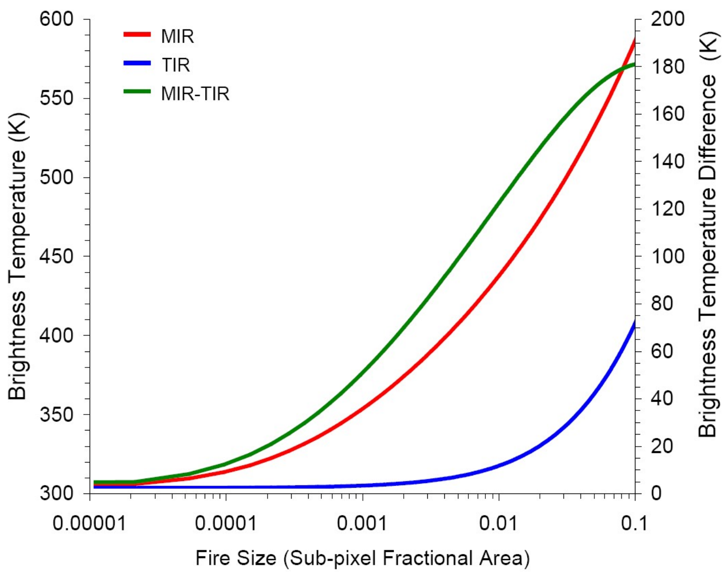

Figure 4. MIR and TIR brightness temperatures for modelled fire pixel. The fire pixel contains an active fire of effective BT 900 K, superimposed on an ambient background of 300 K. As the proportional area of the pixel covered by the fire increases, the BT measured in both spectral channels also increases, but more rapidly in the MIR channel due to the fires spectral radiance signal peaking in this wavelength region. Thresholding of the MIR-TIR BT difference between these two spectral channels is commonly used to detect such active fire pixels. Fires of this temperature covering even 10^{-3} of a pixel are seen to raise the pixels MIR-TIR BT difference by more than 10 K. Emissivity and atmospheric effects have been neglected in this calculation.

2.3 Fire Characterisation Principles

Once an active fire pixel has been detected, it can be characterised through estimation of its fire radiative power. As previously described, FRP quantifies the rate of release of radiant energy by a fire over all wavelengths (albeit primarily in the infrared) and over the viewing hemisphere above the fire. However, SLSTR measures the fire pixel signal in only a few discrete wavebands and in one viewing direction. Two approaches to address the estimation of FRP from such data are the bi-spectral method coupled to the Stefan-Boltzmann Law, which exploits the differential fire signal in two or more co-registered spectral channels (Dozier 1981), or single channel approaches that exploit the signal in the MIR channel only (Wooster *et al.*, 2003). All approaches assume the fire energy emission is essentially lambertian. For the reasons stated earlier, at the present time the SLSTR algorithm will adopt the single channel MIR radiance method for fire characterisation originally presented in Wooster *et al.* (2003) due to its relatively moderate spatial resolution and the influence on the bi-spectral method of background 'clutter' in the TIR channel and its sensitivity to interchannel spatial misregistration effects.

The MIR radiance method is based on a power law approximation to the Planck function (Wooster *et al.*, 2003). The method exploits the fact that for the temperature range of active fires (~ 650 – 1350 K) at MIR wavelengths the Planck function relationship between emitted spectral radiance and emitter temperature approaches a 4th order power law (Figure 5). Since the same fourth order power law is found in Stefan's Law, which relates total energy radiated per second per unit area (i.e. over all wavelengths and over the hemisphere above the surface; so the Fire Radiative Power per unit area) to emitter temperature, the per unit area fire radiative power (FRP_A) can be expressed as a linear function of the fire emitted spectral radiance measured in a MIR spectral band (Wooster *et al.*, 2005):

$$FRP_A = \left(\frac{\sigma . \varepsilon_f}{a . \varepsilon_{f,MIR}} \right) L_{f,MIR} \qquad [Wm^{-2}] \qquad (3)$$

where σ is the Stefan-Boltzmann constant (5.67×10^{-8} $W.m^{-2}.K^{-4}$), ε_f is the broadband emissivity of the fire and ε_{MIR} is the MIR spectral emissivity. Gray body behaviour is at present assumed ($\varepsilon_f = \varepsilon_{f,MIR}$), which is understood to be a realistic approximation for vegetation fires (Langaas, 1995). a ($W.m^{-2}.sr^{-1}.\mu m^{-1}.K^{-4}$) is the power-law scaling constant whose derivation is described in Wooster et al. (2005). $L_{f,MIR}$ ($W.m^{-2}.sr^{-1}.\mu m^{-1}$) is the spectral radiance of the fire itself.

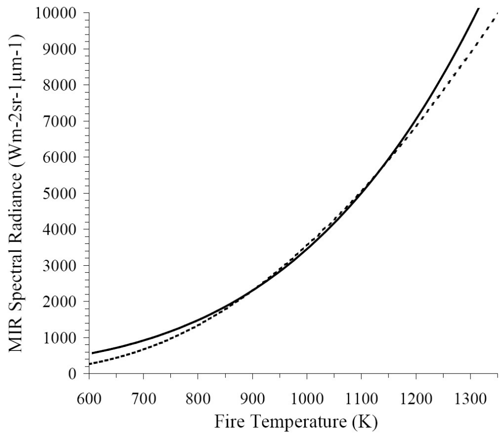

Figure 5. Spectral radiance at MIR and power law approximation. The spectral radiance at is derived from the Planck Function (solid line) and from a fourth order power law (L = aT[4]; dashed line). For the range of emitter temperatures expected to encompass combustion occuring in open vegetation fires (~ 650 – 1300 K) the approximation is correct to within ± 10%.

With the coarse spatial resolution pixels of SLSTR, we cannot directly measure $L_{f,MIR}$ and can only measure the pixel integrated spectral radiance given by the mix of fire and ambient background (Equation 2). Thus $L_{f,MIR}$ is generally estimated as the difference between the MIR spectral radiance of the fire pixel and the mean of the immediately surrounding non-fire ambient 'background' pixels. However, Equation (2) is a gross simplification that neglects many other contributions to the pixel radiance, so these must be included to obtain the full description of the fire pixel radiance to include both emissivity, atmospheric and solar radiation effects. Thus, under the assumption of cloud free conditions, for a pixel containing a sub-pixel sized fire, the at-sensor MIR spectral radiance (L_{MIR}) will be the summation the following terms; emitted fire thermal radiance, solar and atmospheric downwelling irradiance reflected from the fire, emitted thermal radiance from the non-fire background, the solar and downwelling atmospheric irradiance reflected from the non-fire background, and the upwelling atmospheric thermal radiation:

$$
\begin{aligned}
L_{MIR} &= \tau_{MIR} p_f \varepsilon_{f,MIR} B(\lambda_{MIR}, T_f) + \tau_{MIR} p_f (1-\varepsilon_{f,MIR})(\tau_{d,MIR} I_{sun,MIR} \cos\phi + I_{atm,MIR})/\pi \\
&+ \tau_{MIR}(1-p_f)\varepsilon_{b,MIR} B(\lambda_{MIR}, T_b) + \tau_{MIR}(1-p_f)(1-\varepsilon_{b,MIR})(\tau_{d,MIR} I_{sun,MIR} \cos\phi + I_{atm,MIR})/\pi \\
&+ L_{atm,MIR}
\end{aligned}
\tag{4}
$$

where τ_{MIR} is the upward atmospheric transmission in the sensors MIR spectral channel, ϕ is the solar zenith angle, $\tau_{d,MIR}$ is the downward atmospheric transmission in the sensors MIR spectral channel at angle ϕ, $I_{sun, MIR}$ is the extraterrestrial solar irradiance in the sensors MIR spectral channel, $I_{atm,MIR}$ is the diffuse downwelling atmospheric irradiance in the MIR spectral channel, and $L_{atm,MIR}$ is the upwelling atmospheric spectral radiance in the MIR spectral channel. T is land surface temperature, ε is emissivity and p the proportion of the pixel covered by that component, with subscript *f* corresponding to their value at the fire and *b* at the non-fire background.

Similarly for a neighbouring non-fire 'background' pixel:

$$L_{b,MIR} = \tau_{MIR}\,\varepsilon_{b,MIR}\,B(\lambda_{MIR}, T_b) + \tau_{MIR}(1-\varepsilon_{b,MIR})(\tau_{d,MIR}\,I_{sun,MIR}\cos\phi + I_{atm,MIR})/\pi + L_{atm,MIR} \tag{5}$$

The fire emitted spectral radiance in the MIR spectral channel, $L_{f,MIR}$, required as input into equation (3) is in fact the $p_f\varepsilon_{MIR}\,B(\lambda_{MIR},T_f)$ term on the right hand side of equation (4) (i.e. the spectral emissivity of the fire multiplied by its spectral emittance). The value of this term can be obtained numerically by combining Equations (4) and (5) and re-arranging:

$$\begin{aligned} p_f\varepsilon_{MIR}B(\lambda_{MIR},T_f) &= \frac{1}{\tau_{MIR}}\left(L_{MIR} - (1-p_f)L_{b,MIR} + p_f L_{atm,MIR}\right) \\ &- p_f(1-\varepsilon_f)(\tau_{d,MIR}I_{sun,MIR}\cos\phi + I_{atm,MIR})/\pi \end{aligned} \tag{6}$$

The right side of Equation (6) represents the true value of $p_f\varepsilon_{MIR}B(\lambda_{MIR},T_f)$ for use as $L_{f,MIR}$ in Equation (3). Multiplying the output of (3) by the sensor ground field of view then provides an estimate of the fire radiative power in Watts.

However, certain of the parameters in Equation (6) cannot be readily determined, for example the unresolved fire fractional area, p_f, whilst others, for example the atmospheric parameters, are likely to be imperfectly known. By neglecting the (relatively) unimportant terms, Equation (6) can be greatly simplified and then parameterised using the SLSTR measured radiances, in order to provide an estimate of $L_{f,MIR}$ for input into Equation (3).

The first assumption is that the atmospheric term $p_f L_{atm,MIR}$ on the right hand side of Equation (6) will always be small compared to at least one of the first two terms and is therefore negligible. Next, the requirement to know the fire fractional area (p_f) is removed by assuming that $(1-p_f)L_{b,MIR} \approx L_{b,MIR}$, which is considered workable when p_f is sufficiently small. As p_f increases, the error introduced by this assumption remains negligible, since in that case the spectral radiance of the fire pixel will be increasingly dominated by emittance from the (increasingly large) fire rather than from the much cooler ambient background. This is because $B(\lambda_{MIR}, T_f)$ is many orders of magnitude larger than $B(\lambda_{MIR}, T_b)$ at MIR wavelengths (Figure 3). The final term in Equation (6) corresponds to the solar and downwelling atmospheric radiation reflected from the fire, and is assumed negligible for the same reason.

Via these simplifications the fire-emitted spectral radiance ($L_{f,MIR}$) for input into Equation (3) can be estimated from the difference between the MIR spectral radiance of the active fire pixel (L_{MIR}) and that of the surrounding non-fire 'background' ($L_{b,MIR}$), which is generally estimated from the average signal of the valid (i.e. non-fire, non-water, non-cloud) pixels within a 'background window' surrounding the fire pixel. Thus:

$$L_{f,MIR} = p_f \varepsilon_{f,MIR} B(\lambda_{MIR}, T_f) \approx \frac{1}{\tau_{MIR}} \left(L_{MIR} - L_{b,MIR} \right) \tag{7}$$

Combining Equations (3) and (7) we obtain a method for calculating the FRP averaged over a coarse spatial resolution pixel in units of W.m^{-2}. Multiplying by the ground projection of the sensor FOV (A_{sampl}) provides the FRP in Watts:

$$FRP_{MIR} = \frac{1}{10^6 . \tau_{MIR}} \left(\frac{\sigma . \varepsilon_f}{a . \varepsilon_{f,MIR}} \right) \left(L_{MIR} - L_{b,MIR} \right) \quad \text{[MW]} \tag{8}$$

An adaption for gas flares, which are typically much higher in temperature than vegetation fires (>1500K) and which have their spectral radiance peak around the shortwave infrared band (SWIR2; 2.2 μm) of SLSTR (as shown in Figure 3), means that the FRP of Gas flares is best calculated at night using the excess spectral radiance assessed in the SWIR2 band, rather than the MIR band:

$$FRP_{SWIR} = \frac{1}{10^6 . \tau_{SWIR}} \left(\frac{\sigma . \varepsilon_f}{a . \varepsilon_{f,SWIR}} \right) \left(L_{SWIR} - L_{b,SWIR} \right) \quad \text{[MW]} \tag{9}$$

During the daytime, strong solar reflected signals in the SWIR dominate over most thermally emitted signals, and mean that use of Equation 9 is confined to night-time situations, unlike Equation 8 which operates both day and night.

3 ALGORITHM DESCRIPTION

3.1 Overview of Algorithm Structure

The SLSTR Active Fire algorithm can be considered a Six-stage process, outlined in Figure 8. The stages are applied to SLSTR data that has already been cloud masked and separated into two subsets based on geographic location, namely the land area potentially capable of supporting land based hotspots (i.e. the land surface with the locations of larger lakes and rivers masked out) and the ocean areas that might potentially be the sites of ocean hotspots, i.e. offshore gas flares (i.e. this assumes that processing data of the entire open ocean would be computationally wasteful and is to be avoided where possible). The Sentinel-3 SLSTR channel naming convention and the matching scientific notation used throughout this document is shown in Appendix A.

Note that whilst the SLSTR active fire (AF) detection and fire radiative power (FRP) retrieval algorithm uses data from many of the SLSTR spectral channels, it is mainly reliant on data from the MIR 3.7 µm channel (Channels S7 and F1) and thermal infrared (TIR) 10.8 µm channel (Channels S8 and F2). The precision of the BT measurements in the "normal" range (273-311 K) in the 'standard' MIR and TIR bands (S7 and S8 respectively) is considerably better than that in the dedicated 'fire' channels (F1 and F2). However, non-linearity of the S7 band has been noted above a recorded BT of around 311 K and full saturation of the channel at a reported brightness temperature of around 312 K, significantly lower than 323 K originally specified. This makes S7 quite commonly saturated over hotter ambient land surfaces, and very often saturated over active fires, and F1 is therefore required to be used in the AF detection and FRP retrieval process more commonly than expected pre-launch. This has made the algorithm included herein far more complex than that described pre-launch in Wooster et al. (2012), especially since the F1 detectors are not co-incident on the focal plane with the 'S' band detectors, and have a different ground FOV and orientation compared to S7 which makes the data of S7 and F1 more difficult to use together. To cope with this, a clustering algorithm has had to be used that uses the AF detections made in the S7 band, clusters them into those AF pixels belonging to a single "fire", identifies that same fire in the F1 channel, and then identifies all the F1 AF pixels belonging to that fire. This approach is described in Section 3.2.5. Furthermore, the pixel area of the F1 pixels is also more consistent across the swath, and for much of the swath also smaller than for S7 (Figure 6). This relatively smaller and more consistent pixel area makes F1 attractive for FRP estimation, and potentially provides an ability to detect smaller fires than with S7 (Wooster et al, 2015, Freeborn et al, 2014), albeit the spatial offset between the F1 band and the S8 band needs to be overcome.

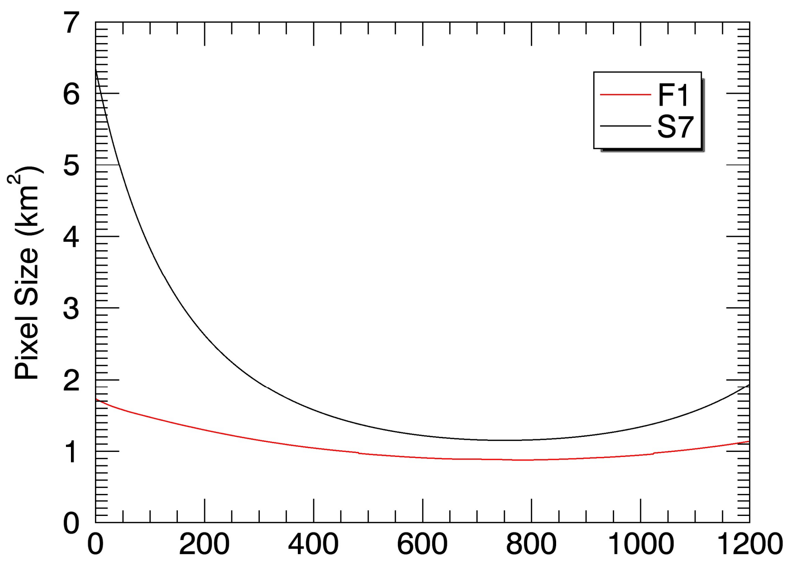

Figure 6. Pixel area (km^2) of the SLSTR F1 and S7 channels across the nadir swath. Note the F1 has more consistent pixel area across the swath than S7, increasing from 0.9 km^2 to 1.8 km^2 at the far-left swath edge compared to 1.1 km^2 to 6 km^2 for the S7 channel. Pixel size data courtesy Science and Technology Facilities Council (STFC) Rutherford Appleton Laboratory.

The different pixel sizes of F1 and S7 provides also different image characteristics when fires are viewed by these two Channels, especially at the far-left edge when the pixel area of S7 is nearly six times that at nadir. At this far-left swath edge, any fire seen by S7 will be greatly oversampled in a manner similar to the so-called "Bow-Tie" effect of MODIS (Giglio et al., 2003). The effect is far less in the smaller F1 pixels. Figure 7a and Figure 7b shows the same fire viewed by F1 and S7 at a view zenith angle of 52° (far-left swath edge). Whilst F1 shows effectively only one strong active fire pixel with an FRP of 10.8 MW, S7 shows eight pixels (three cosmetically filled) with a total FRP of 25.2 MW from the five discrete and unique non-cosmetically filled pixels. Figure 7c and 7d further illustrate this issue using a simulation of the far-left swath edge. Here an 800 K active fire with a size of 1600 m^2 (0.16% of a 1 km^2 pixel) is used as a target, superimposed on a homogeneous background of 290 K (FRP = 37.2 MW). Simulations conducted with the SLSTR pixel area and scan geometry indicate that in the F1 channel at the swath-edge this fire would result in only one active fire pixel (F1 BT of 334.5 K) being detected by the SLSTR active fire detection algorithm, detailed herein (with an FRP of 35.6 MW, very close to the true value), whilst for S7 three active fire pixels would be detected due to pixel overlap, with BTs of 310.5, 306.2 and 311.9 K (after removing cosmetically filled pixels) and a total FRP of 94.2 MW. This is ~ 2.5× the FRP recorded by F1 for the same fire, which is the same situation found in the real data of Figure 7a,b.

In real SLSTR data and in simulations, fires lying close to the nadir view swath edge affect far fewer pixels in F1 than in F7 (Fig. 7), which enables F1 to potentially provide improved FRP estimates less affected by double or triple counting. To make full use of this potential F1 channel benefit, the algorithm proposed here uses a switch (F1_switch) which, when set to "ON", means that all FRPs are calculated from F1 measured spectral radiances and reported at the F1 pixel location for all the AF pixels. If the F1_switch is set to OFF, if any single fire contains multiple AF pixels and any one of them are in the non-linear or saturated region of S7 (i.e. $\geq S7_{AT}$; which is expected to be set to 311 K) then the FRP retrieval for all the AF pixels will be conducted using F1, but otherwise FRPs are derived from S7-recorded spectral radiances. This is discussed further in Section 3.2.5, and the effectiveness of operating this "switch" in the ON or OFF position will be studied in detail once the processing chain has been completed. The aforementioned clustering procedure is a necessary part of this processing, whether the F1_switch is set to ON or OFF.

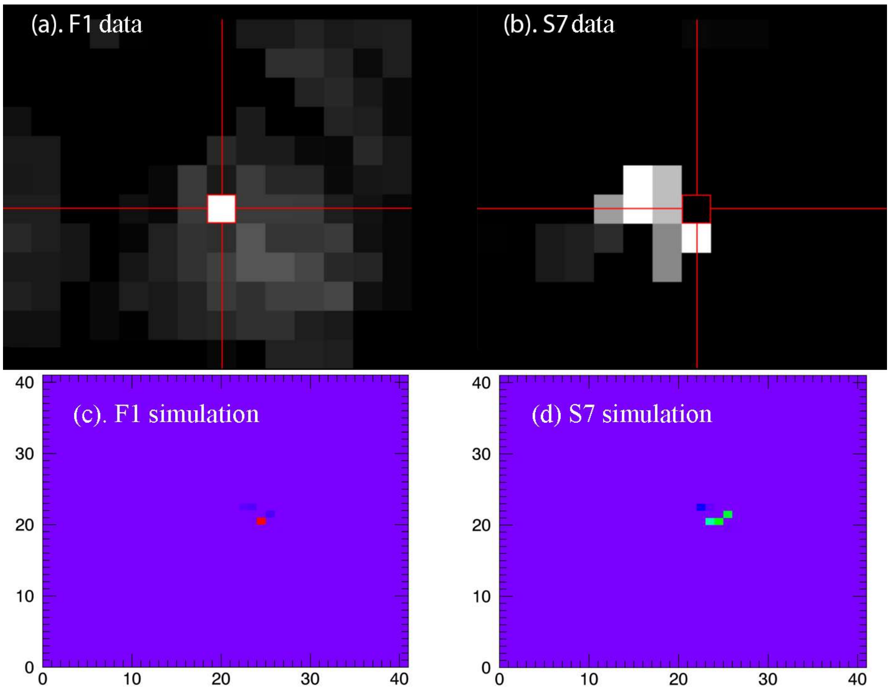

Figure 7. Different shape and size of the same active fire recorded simultaneously by F1 and S7 SLSTR spectral channels, which operate at the same middle infrared wavelength but with different pixel size and overlap characteristics (see Figure 6). (a, b) Real SLSTR data, (c, d) simulated data of an 800 K active fire with an area of 1600 m² imaged by S7 and F1 towards the left-hand swath edge. In both the real data and the simulations the active fire pixels appear oversampled in S7 compared to F1, and the retrieved FRP using the S7 active fire pixels is more than twice that retrieved using F1. Simulations based on code provided by the Science and Technology Facilities Council (STFC) Rutherford Appleton Laboratory.

Note also that the VIS to SWIR (reflected solar radiation) channels S1 to S6 of SLSTR are recorded at a 500 m nadir spatial resolution, whereas the thermal (MWIR and LWIR) channels have a 1000 m spatial resolution at nadir. The SLSTR Active Fire algorithm uses data from both types of channel, and this needs to be taken into account of during data processing where measurements from both types of channel are used (e.g. in a band ratio). Where the SWIR channels are used alone in a night-time test, it is desirable to undertake the analysis at the original 500 m spatial resolution since the hotspot signals will be maximized at this smaller pixel area. This enables the algorithm to be most sensitive to the smaller sub-pixel hotspots, though final output from the product is delivered on a 1 km grid. The re-mapping method to go from the 500 m pixels to the 1 km grid is detailed in Section 3.2.3, but essentially represents a coordinate division by two. However, this does not always find exactly the same AF pixel in S7 as in S6, so the aforementioned clustering approach is also used here.

The six active fire pixel detection stages utilize a series of spatially varying thresholds to detect the set of confirmed fire pixels in the scene under consideration, with the thresholds varying between day and night conditions. Furthermore, the thresholds vary between the detection of hotspots on land and over the ocean. Nighttime pixels are those defined as having a solar zenith angle ≥ 85 °. By day, solar reflected radiation from cloud tops or edges can lead to high MIR signals at cloud-contaminated pixels, whereas the clouds will typically be cold and thus have a low TIR signal. Therefore T_{MIR}, T_{TIR} and $\Delta T_{MIR-TIR}$ recorded at certain cloud-contaminated pixels may appear similar to those of fire pixels. Furthermore, inland water bodies (lakes and rivers), together with mixed land-water pixels at coastlines, can be expected to have rather different MIR and TIR brightness temperatures to the neighboring land surface pixels, and might also be affected by specifically reflected sunglint. Therefore the availability of an accurate cloud mask and land/water mask is very important for the fire application, and only SLSTR pixels that have been confirmed as clear-sky, land pixels via the use of such masks should be used within the land hotspot tests. Of course, some small or seasonally varying water bodies may not be present in the land-water mask, and small or semi-transparent clouds may not be identified by the cloud mask. To assist in these instances the active fire detection algorithm contains some simple tests that aim to reduce problems introduced by such cases. Masks of "(semi-) permanent high temperature events" (e.g. gas flare, volcanoes) will also be applied after fire detection in order to separate such detections from true vegetation fires in terms of hotspot type classification.

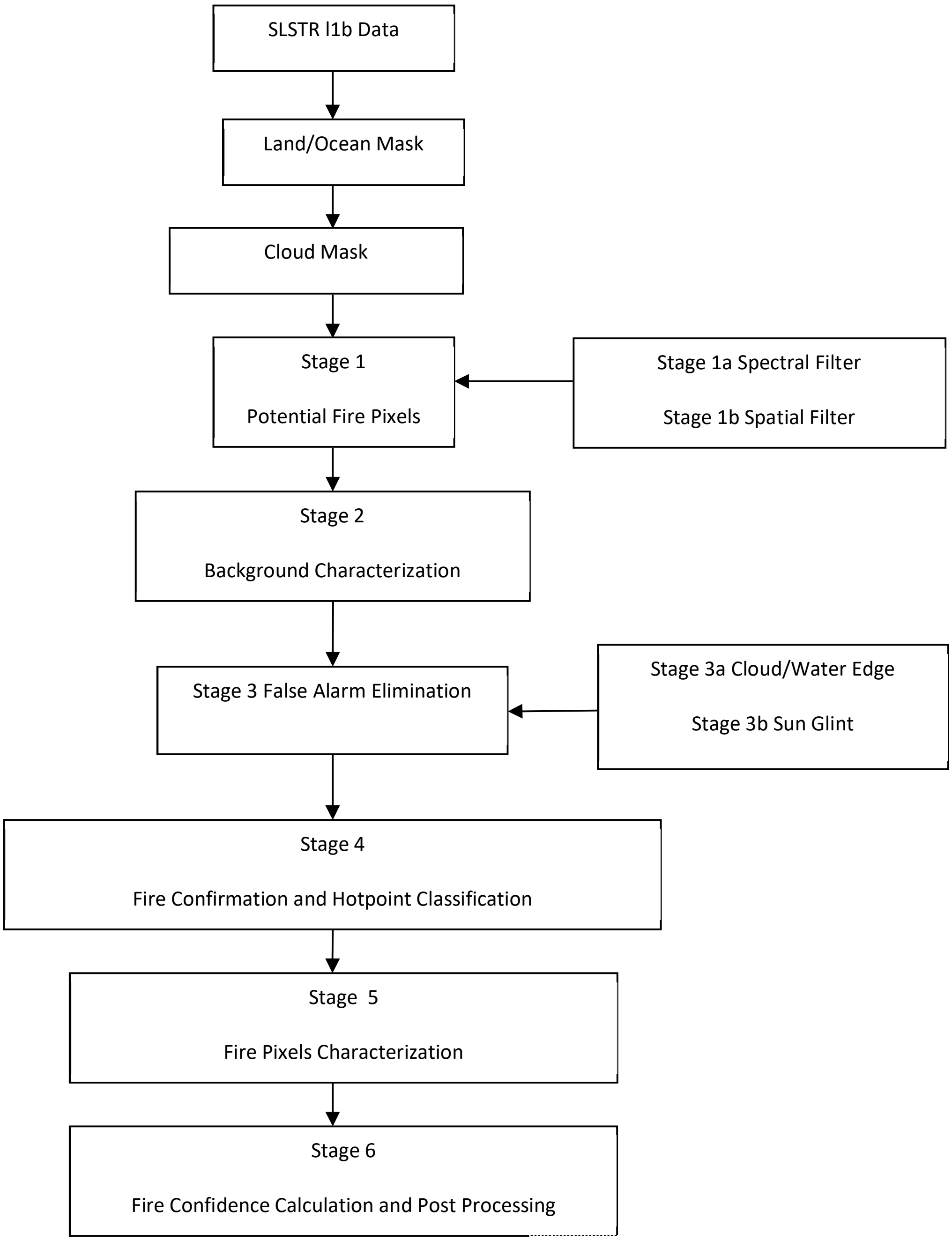

[See overleaf for caption]

Figure 8. Structure of the SLSTR Fire Detection and Characterisation algorithm (prior page). Note the algorithm has evolved further from the pre-launch version presented in Wooster *et al.* (2012), for example to include detection of offshore hotspots. Prior to Stage 1 fire detection commencement, two separate geographic subsets of data would need to be determined: namely the cloud-free land area potentially capable of supporting land based hotspots (i.e. the land surface with the locations of clouds, larger lakes and rivers masked out) and cloud-free ocean areas that might potentially be the sites of offshore gas flares. Each of the stages is then applied to each of the two geographic subsets of data, though with some alterations to the thresholds used, and in a few cases some tests being de-activated or added. The only exception is Stage 4b 'desert elimination' which is not necessary over the ocean or over the land at night. For both geographic subsets, thresholds and test details can vary between observations made under night-time and daytime conditions.

3.2 Land hotspots Detection

Firstly, all cosmetic fill pixels from the nadir view S2, S6, S7, S8 and F1 channels are masked out so they are not used within the AF detection and FRP characterization process. These cosmetic fill pixels should be excluded in the potential AF detection processing, including the spectral filter and spatial filters, and should also be excluded from the FRP retrieval process including the background characterization.

3.2.1 Detection of Potential Fire Pixels (Stage 1)

The purpose of this stage is to identify all pixels whose spectral and spatial signals suggest that they may potentially contain an actively burning vegetation fire. The aim is to successfully include all the true fire pixels within the potential fire pixel set, whilst minimizing the number of non-fire pixels included so as to minimize data processing overheads and avoid later false alarms. A spectral filter using a set of spectral thresholds is applied to detect a set of potential fire pixels P_1, based on their thermal channel BT signals. In some circumstances, much of the cloud-free land surface maybe returned as a potential fire pixel by the spectral filter, particularly when thresholds are set low so as to minimize errors of omission (i.e. the missing of fire events). For this reason, a spatial (edge detection) filter is used to detect a second set of potential fire pixels P_2, based on the spatial variation of $\Delta T_{MIR\text{-}TIR}$, and the final set of potential fire pixels P_f is based is the intersection of these two:

$$\mathcal{P}_f \in \left\{ \mathcal{P}_1 \cap \mathcal{P}_2 \right\} \tag{10}$$

Spectral Filter Detail (Stage 1a)

Stage 1a identifies potential fire pixels belonging to set P_1 using two adaptive thresholds. Firstly, the scene is divided into equal sized sub-scenes having dimensions in terms of along- and across-track coordinates. The dimensions can be adapted as further experience of real SLSTR data is gained over time, but we suggest one half of the sensor swath width is used in the first instance. For each sub-scene being tested, the number of land (N_{land}) and cloud free land (N_{cf_land}) pixels is calculated. The subscene is classified as valid for use in adaptive threshold determination if the number of land pixels is greater than 10% of the total number of pixels in the subscene, and if the number of cloud free land pixels is greater than 1% of the total number of pixels in the subscene. In this case the mean values of T_{S7}, T_{S8} and $\Delta T_{S7\text{-}S8}$ for all cloud-free land pixels in that subscene are used as the spectral filter thresholds ($\overline{T}_{S7}^{cf}$, $\overline{T}_{S8}^{cf}$ and $\overline{\Delta T}_{S7-S8}^{cf}$ respectively) against which each cloud-free land pixel in the subscene is tested for inclusion into potential fire pixel set P_2 :

$$T_{S7} > \overline{T}_{S7}^{cf} + p \times \vartheta_s \qquad (11a)$$

where p = -0.3 for day and p=0 for night

and

$$\Delta T_{S7-S8} > \overline{\Delta T}_{S7-S8}^{cf} \qquad (11b)$$

θ_s is the solar zenith angle (in degrees), and use of this parameter enables adjustment of the S7 band detection threshold to cope with the fact that at locations where the solar elevation is high, the ambient background temperature and the solar reflectance component of the S7 signal are typically greater. All parameters in these tests come from previous applications of the same tests made using SEVIRI or MODIS (e.g. Wooster et al., 2015; Giglo et al., 2003; 2016), updated with testing using real SLSTR data.

Tests (11a) and (11b) are targeted at identifying the spectral signature of fires, whose pixel integrated S7 BT and S7-S8 BT difference should in general be higher than those of the subscene ambient background. Using adaptive thresholds for the detection of potential fire pixels, rather than fixed thresholds such are used in the MODIS fire product (e.g. $T_{S7} > 310$ K and $T_{S7\text{-}S8} > 10$ K; Giglio *et al.*, 2003) provides the algorithm a chance at identifying the more weakly burning and/or smaller component of the fire regime – which can be rather numerous in areas such as disturbed tropical forests. The disadvantage is that many more non-fire pixels may also be returned, and

If N_{land} and/or N_{cf_land} are too low to meet the 10% and 1% criteria specified above, then the weighted mean of the spatial filter thresholds $\overline{T}^{cf}_{S7}$, $\overline{T}^{cf}_{S8}$ and $\overline{\Delta T}^{cf}_{S7-S8}$ calculated from the (maximum five) valid spatially neighboring subscenes are used (with the weighting for each subscene given by its value of N_{cf_land}). If no valid neighboring subscenes are available, which we expect to be relatively rare over most land areas given the non-stringent requirement for only 1% of land pixels to be cloud free, then default thresholds are used:

By day,

$$T_{S7} > 310\ \mathrm{K} + p \times \theta_s \quad (11c)$$

Where p = -0.3

and

$$\Delta T_{S7-S8} > p \quad (11d)$$

where p = 5 [Kelvin]

By night,

$$T_{S7} > p \quad (11e)$$

Where p = 290 [Kelvin]

and

$$\Delta T_{S7-S8} > p \quad (11g)$$

where p = 3 [Kelvin]

Pixels failing these preliminary tests are immediately classified as non-fire pixels. Pixels passing these tests belong to set P_1 relate to the land area.

Warmer land areas will certainly have many pixels saturated in S7, and this effectively hinders detection of active fires in such locations since the presence of fire cannot increase the S7 BT any higher than it is already. The F1 channel can potentially be used to circumvent this issue, but at the current time the data from this channel is somewhat spatially offset from that in the S8 channel, and thus it is non-trivial to use these two bands together in e.g. a contextual AF detection algorithm designed to be sensitive even to relatively small/low FRP fires. Therefore, at present areas with too much S7 saturation are masked out as not-being able to be processed for the active fire application. This will remove many daytime scenes, but is not expected to impact many nighttime scenes. To conduct this masking, at this stage of the processing the number of pixels in the sub-scene being analysed having an S7 brightness temperature exceeding the pre-set threshold beyond which S7 is considered inaccurate ($S7_{AT}$, currently expected to be 311 K) is recorded (N_{af_land}). This number is compared to the total number of cloud free land pixels in the sub-scene (N_{cf_land}), and if their fraction exceeds a pre-set threshold ($Classic_{day\_fraction\_threshold}$, currently set as 0.01[1%]), the sub-scene will be considered to have too many background pixels having $T_{S7} > S7_{AT}$ to be processed further (apart from for the absolute threshold AF detection test, which is based on F1 not S7). This 1% threshold has been selected from testing of SLSTR data available currently over fire affected areas. A sub-scene is extremely unlikely to have enough active fire pixels to cause this threshold to be exceeded, and so it is considered a simple but effective method of identifying sub-scenes containing many saturated S7 pixels, sub-scenes interpreted to have ambient background pixels which are very frequently saturated in the S7 channel and which cannot therefore be processed with the 'classic' daytime algorithm. An algorithm evolution to deal with the non-classic case, where S7 is saturated over even the background pixels, will be introduced at a later stage.

Spatial Filter Detail (Stage 1b)

The spectral filter of Stage 1a is designed to be very liberal (in order to catch any possible AF pixels), with the disadvantage that it can return very large numbers of potential fire pixels many of which are not fires. Such pixels include those containing large areas of solar-heated bare rocks, soil or other "warm" surfaces, such as are found in arid or desert areas for example. In order minimize the inclusion of such areas in the final potential fire pixel set (P_f) and so reduce potential commission errors and computational cost, a series of spatial thresholds is employed in conjunction with an edge detection filter. This test is used to identify locations where the $\Delta T_{S7\text{-}S8}$ signal shows a marked spatial change such as is found at fire pixels but not at areas of homogeneous warm land. A series of high-pass filters **K** are applied to $\Delta T_{S7\text{-}S8}$ to identify a second potential fire pixel set P_2 [with, as before, one P_2 for land areas and one P_2 for ocean areas]. Since the contrast between fire and non-fire pixels is greater in $\Delta T_{S7\text{-}S8}$ than in the MIR channel alone, the spatial filter is applied to the brightness temperature difference data (Roberts and Wooster, 2008).

The idea behind the use of the high pass spatial filter is that since each SLSTR pixel measures the spatially averaged radiance over ~ 1 square kilometer, ΔT_{S7-S8} recorded at non-fire "background" pixels generally changes rather gradually from pixel to pixel. In contrast, a pixel containing an active fire represents a high spatial frequency change in $\Delta T_{S7-S8,}$ which can thus be isolated via a high-pass spatial filter. Filter kernels of size f_K x f_K are used, where f_K is taken sequentially as 3, 5, 7 and 9, with the 3 x 3 filter having the coefficients shown in Figure 9.

-1	-1	-1
-1	8	-1
-1	-1	-1

Figure 9. Coefficients of the 3 x 3 high pass spatial filter.

The use of multiple filter kernel sizes attempts to ensure that the spatial filter is appropriate for detecting both single fire pixels and those belonging to larger spatial clusters of fire pixels. The edge detection filter is applied to the entire scene, and pixels passing the test are those where the filter output (h_K) exceeds a threshold defined in relation to the filter output standard deviation calculated from all the clear sky, land surface pixels in the SLSTR subscene within which the test pixel resides. A subscene has the same definition as in Stage 1a.

$$P_2 \in \{h_K \geq p \times \sigma_{fK}\} \qquad (12)$$

where p = 1.5

Where σ_{fK} is the standard deviation (Kelvin) of the clear sky, land surface pixels in the subscene, high-pass filtered with filter size f_K, and p is the threshold multiplier taken as 1.5 currently. We use the same criteria for defining valid subscenes as per Stage 1a, and for calculation of the thresholds in the case that the current subscene under consideration fails to contain sufficient cloud free, land pixels. In the case where there are no valid subscenes available for a particular fire pixel (which is expected to be a rare occurrence), default values of 3 for σ_{fK} are used instead, for all the filter sizes.

A pixel having $\Delta T_{S7\text{-}S8}$ belongs to set P_2 if condition (11) is valid for at least one of the four filter kernel sizes f_K.

Stage 1 selects the final potential fire-pixel set as those pixels passing both Stages 1a and 1b. In the subsequent stages these pixels will then be further tested to confirm whether they do in fact contain an active fire. As with other stages, the processing is conducted independently for land and ocean geographic subsets, so two potential fire pixel sets are ultimately produced, those corresponding to the land and those corresponding to the ocean respectively.

3.2.2 Background Characterisation (Stage 2)

The objective of the background characterization step is to provide an estimate of what the radiometric signal of the potential fire pixel would be in the absence of fire, based on statistics derived from the set of valid "background" pixels P_b located within a window W of size b_W x b_W immediately surrounding the potential fire pixel being tested. Stage 3 will use this estimate to determine whether the observed potential fire pixel signal is sufficiently different to this value such that it can be confirmed as a true fire pixel.

At each potential land fire pixel belonging to set P_f, b_W is initially set as 5. The center pixel of this 5 x 5 window is the potential fire pixel itself and so is discounted, and the immediately surrounding eight background pixels are also discounted since their closeness to the potential fire pixel can result in their radiances being contaminated by the fire radiance itself. Thus for the 5 x 5 sized window, a total of 16 pixels are initially included. From these 16 pixels, the set of valid background pixels P_b are selected based on their being identified as clear-sky, land pixels that for daytime observations are not influenced by strong sun glint and which have:

$T_{S7,w} < T_{S7,pf}$ (13a)
$\Delta T_{S7\text{-}S8,w} < \Delta T_{S7\text{-}S8,pf}$ (13b)
$T_{S7,w} < p$ (13c)

Where p = 311 [K]

$\Delta T_{S7\text{-}S8,w} < p$ (13d)

Where p = 20 [K]

$\theta_g < p$ (13e)
where p = 2 [degrees]

Where $T_{S7,w}$ *and* $\Delta T_{S7\text{-}S8,w}$ are the middle infrared brightness temperature and the brightness temperature difference of the pixel in the background window respectively; $T_{S7,pf}$ *and* $\Delta T_{S7\text{-}S8,pf}$ is middle infrared brightness temperature of the potential fire, θ_g is sun glint angle, which is defined in Equation 14 and which is used here to ensure that the background pixels are not in a region of the Earth that could be affected by sunglint. The purpose of tests 13a-13e is, as far as possible, to remove other fire pixels from the background pixel set and to thus select P_b as being representative of the uncontaminated ambient background signal. For nighttime observations, the sun glint test is not required and the thresholds for test 13c and 13d are lowered to 310 K and 10 K respectively.

If the number of valid background pixels in set P_b is no less than 25% of the total number of background pixels (excluding from the total number of background pixels the potential fire pixel itself and the 8 immediate surrounding pixels; so 16 pixels for the smallest b_W of 5) [and for the smallest b_W of 5 the total number of pixels is eight or more] then the background window statistical characterization process proceeds immediately using a window size b_W of 5. If this condition is not met, the window size b_W is increased through 7, 9, 11, 13,15, 17, 19 and 21 and the test repeated at each stage until the conditions are met. For each window size the 8 pixels spatially neighboring the potential fire pixel itself (along with the potential fire pixel being tested and any other potential fire pixels within the window, so the total excluded number of pixel will be 9) are excluded from the background pixel set, and thus for example the maximum number of background pixels in the case where $b_W = 7$ is 40 (7*7 - 9).

If an insufficient number of valid neighboring pixels is identified using even the 21 x 21 window, the background characterization is unsuccessful and the fire pixel is classed as "unknown". The approach inherently assumes that the spatially closest pixels to the potential fire pixel being tested have a signal most similar to that which the potential fire pixel would have in the absence of fire. The 21 × 21 background window maximum size, though somewhat arbitrary, ensures that the background signal is sampled within ~ 11 km of the potential fire pixel location, a scale that (Giglio *et al.*, 2003) found empirically to be appropriate for preventing false alarms induced by the unrepresentative selection of background pixels.

Following Giglio *et al.* (2003) the number of valid background pixels within the background window is recoded as N_b. The number of pixels excluded from the background window is also recorded for later use in false alarm reduction and in defining the fire pixel confidence measure. The number of pixels (N_f) excluded as being "background fires" is set as the total number failing test 13c and test 13d, and the number excluded as being water/land pixels (in the land/ocean hotspot testing respectively) or cloud-contaminated pixels is recorded as N_w and N_c respectively.

For each potential fire pixel where a sufficient number of valid background pixels are identified (which is the vast majority or cases), the background characterisation is classed as successful and a number statistical measures computed from the valid background pixel set P_b. These are $\overline{T}_{S7}$ and σ_{S7}, the respective mean and mean absolute deviation of T_{S7} ; $\overline{T}_{S8}$ and σ_{S8}, the respective mean and mean absolute deviation of T_{S8} ; $\overline{\Delta T}_{S7-S8}$ and $\sigma_{\Delta T_{S7-S8}}$, the respective mean and mean absolute deviation of ΔT_{S7-S8}, and by day $\overline{R}_{S1/S7}$ the mean ratio of the MIR and RED (0.86 micron) radiance calculated over the valid background pixel set.

3.2.3 False Alarm Elimination (Stage 3)

Locations having a radiometrically strong spatial contrast across a geographic boundary in the S7 and S8 channels can potentially cause either errors of omission or commission for a contextual AF detection algorithm. Cloud/Water edge and desert boundaries are the most common features to induce such false alarms. Strong radiance from sun glint also causes false alarms. Since S7 signals become unreliable after $T_{S7} > 311$K, and desert areas may in reality exceed this BT, we will deal with desert boundaries in the future.

3.2.3.1 Cloud/water edge rejection (Stage 3a)

Potential active fire pixels located next to a "Cloud/water" pixel are currently recommended to be disregarded from further processing, since experience shows that a large proportion of these are false detections caused by the spectrally varying signatures of undetected cloud or land–water boundaries. If there is one or more cloudy pixels in the immediately surrounding 3 × 3 pixel window, the AF pixel is recommended to be rejected as cloud edge false alarm if the potential fire pixels MIR brightness temperature (BT) is less than a pre-set threshold 311K for daytime–originally expected to be 330 K (which in fact will never be reached in S7) and 310 for nighttime. Similarly, if there one or more water pixel in the surrounding 3 × 3 pixel window that are water pixels, and if the potential fire pixels MIR BT is less than the 311 K at daytime and 310 K at nighttime, then the AF pixel is rejected as a water edge false alarm. For the gas flare detection on the ocean, if there is one or more land pixel in the 3 × 3 window that are land pixel. These pixels discounted by these tests are flagged as CLOUDEDGE and WATEREDGE (LANDEDGE in the ocean) respectively. Whilst these test limits the number of false AF detections associated with unmasked cloud edges and water bodies, they will likely result in a number of "true" active fire pixels going undetected if they lie next to water bodies or cloud identified by the land/sea and cloud mask. As cloud and water masking with SLSTR become more mature, these tests can potentially be considered for removal from the AF detection algorithm.

As the basic cloud masking and landcover is using in the algorithm, there are undetected cloud and water pixels in the scene, those pixels had been found cause false alarm. Therefore, further tests are needed to remove these false alarms. At daytime, the spectral radiance ratio between S7 and S2 and the ratio between S7 and S8 are employed in the test below, if a potential fire pixel has a BT < 311k and the ratio between S7 and S2 is less than 0.018 or the S7 and S8 ratio less than 0.08, the pixel will be removed and classed as CLOUDEDGE.

$$\frac{L_{S7}}{L_{S2}} < p1 \text{ or } \frac{L_{S7}}{L_{S8}} < \text{p2} \qquad (13f)$$

Where p1 = 0.018 and p2 = 0.08

For the nighttime scene, if there is one or more cloud contaminated pixel in the background window (i.e. Nc > 0), the spectral radiance ratio between the S7 and S8 bands is employed in Equation 13g to further remove false alarms arising around cloud edges. If this ratio is less than 0.05 at the potential AF pixel under test and the AF pixel has a BT < 310K, then it is classed as CLOUDEDGE and removed from further processing.

$$\frac{L_{S7}}{L_{S8}} < \text{p1 and S7} < \text{p2} \qquad (13g)$$

Where p1 = 0.05 and p2 = 310K

Note that it is possible that Test 13f-g can be discarded if a good enough cloud mask is available to use.

3.2.3.2 Sun Glint Identification (Stage 3b)

By day, sun glint over small-unmasked water bodies or cloud, or even from areas of wet or sometimes bare soil, can increase the MIR pixel signal considerably above the TIR signal and lead to false alarms. Such instances are rejected using a scheme based on a combination of those in Giglio (2003) and Zhukov *et al.* (2006), using the glint angle (θ_g) calculated between the sensors viewing direction and the direction of the sun rays specifically reflected from the horizontal (usually water) surface:

$$\theta_g = \cos\theta_v Cos\theta_s - \sin\theta_v \sin\theta_s \cos\theta_\phi \qquad (14)$$

Where, θ_v and θ_s are the view and solar zenith angles respectively, and θ_ϕ is the relative azimuth angle between them.

The following conditions are then evaluated:

$$\theta_g < \text{p} \qquad (15a)$$

Where p = 2 [degrees]

$\theta_g <$ p1 and $\rho_{RED} > p_2$ (15b)

Where p1 = 8 [degrees] Where p2 = 0.15

$\theta_g <$ p1 and $L_{S7} / L_{S2} <$ p2 (15c)

Where p1 = 8 [degrees] and p2=0.01

Tests 15a and 15b reject as false alarms all active fire pixels in the strongest region of potential glint, based on them having a small glint angle, or which have very high RED reflectance values. Test 15c also rejects daytime active fire pixels in the less intense glint region, but which show an insufficiently large ratio of S7 to S2 spectral radiance (since only the MIR channel signal will be increased substantially by a fire, whereas both will be increased by glint). However, this test can only be applied at pixel where T_{S7} is less than or equal to the $S7_{AT}$ threshold at which accuracy degrades considerably (currently 311 K).

The same strategy for glint identification is used for land and oceanic hotspots.

3.2.4 Fire Pixel Confirmation (Stage 4)

This stage uses the statistics from the potential fire pixel and the matching background window to confirm whether or not the potential fire pixel actually contains an active fire. An absolute threshold and a series of contextual thresholds, varied on the basis of the background window statistics, are employed.

3.2.4.1 Absolute Threshold Test

Prior to the series of contextual tests, an absolute threshold test is used to identify the most radiant active fire pixels in a scene. Such a test maybe required for example if a high intensity fire pixel is located within a very large cluster of surrounding fire pixels, from which it has proven impossible to gain a sufficient number of valid background window pixels, or where the background window statistics have for some reason become contaminated by radiance from the immediately surrounding fires. We use the absolute threshold test initially used by Kaufman *et al.* (1998) and still used within the MODIS fire detection algorithm. For daytime pixels a potential fire pixel is confirmed as a true fire pixel (even if at Stage 2 it was classed as "unknown") if:

$T_{F1} > p$ by day (16a)

Where p = 360 [Kelvin]

$T_{F1} > p$ by night (16b)

Where p = 320 [Kelvin]

Thresholds in test 16a and 16b are chosen on the basis that no ambient non-fire pixels are expected to attain these high brightness temperature due to thermal emission and daytime near lambertian reflection of MIR wavelength solar radiation. However, as Giglio *et al.* (2003) points out, despite the high daytime threshold, by day the use of this test must be accompanied by adequate sun glint rejection, otherwise sunglint false alarms may occur.

Since the S7 channel saturates above 311 K, both tests 16a and 16b are applied to data from the F1 channel rather than S7. However, due to the spatial offset between S7 and F1 (even after ortho-geolocation) the location of any AF pixel identified by these two tests applied to the F1 band data may be different than if the same AF were detected by S7. Furthermore, the shape and size of the same 'fire cluster' can also differ between F1 and S7 (see Figure 7), a 'fire cluster' being defined as a group of spatially-connected AF pixels (e.g. Figure 9a). For this reason the FRP calculation and the reported coordinates of all AF pixels belong to a 'fire cluster' having one of more active pixels detected with Test 16a or 16b will be reported at the locations of the relevant F1 pixels (i.e. the F1 image domain), and these AF pixels are classified as "Detected by F1". The entire clustering approach is described in Section 3.2.5.

If some AF pixels in a fire cluster have a signal strong enough to be detected with the contextual detection approach as well as the absolute threshold test, then adjustment maybe needed to avoid double counting. As shown in Figure 10, two AF pixels (A and B) are detected by the absolute threshold test in this large fire cluster – and then other pixels are detected around them based on the "F1 contextual detection" approach described in Section 3.2.5 - but these pixels are also detected with the standard S7 based contextual detection tests, so those duplicated pixels should be removed to avoid the double counting issue. In the event of larger active fire clusters, there maybe two or more AF pixels in the cluster that are detected with the absolute threshold test, but they maybe spatially separated from one another. When the AF clustering around each of these absolute fire pixels is conducted (as detailed in Section 3.2.5), the same AF pixels surrounding them could be detected twice or even more. These duplicated AF pixels should also therefore be removed. Also shown in Figure 10, A and B denote the two AF pixels detected with the absolute threshold test in F1. When A is detected, the whole cluster of F1 AF pixel are subsequently also detected using the "F1 contextual detection" - including B which was also detected by the absolute threshold test. When B is detected, the whole cluster is also detected, including pixel A. Therefore, all these duplicated AF pixels should be removed from the final set of AF pixel results. In the case of F1 "ON" or "OFF" this is done by removing the contextually detected AF pixels from the S7-deteted AF pixel set if they belong to the same AF cluster as the F1 detection.

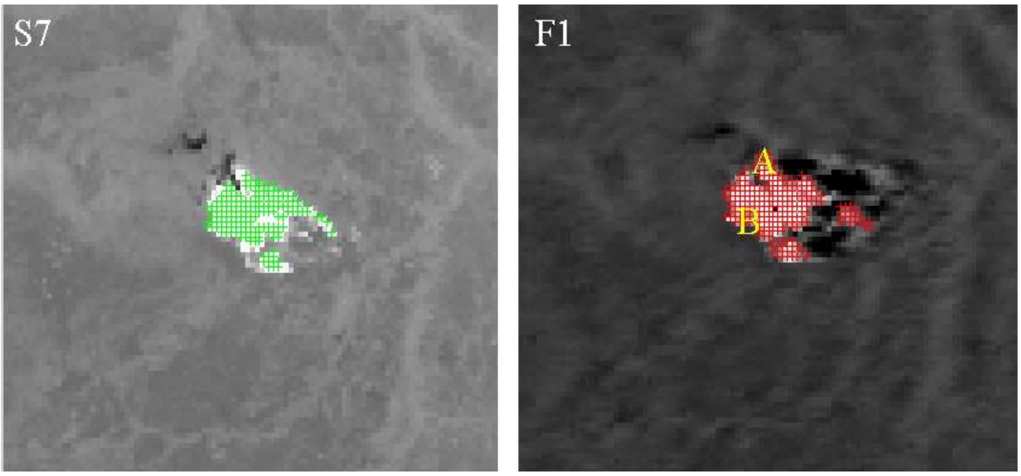

Figure 10. Night-time large-scale fire, containing two pixels (A and B) detected by the absolute threshold test. At left, the green markers represent the S7 contextual AF pixel detections, whilst at right the red markers represent the AF pixel detections in F1 based on the two absolute threshold detections at A and B and the identification of the other F1 AF pixels based on the clustering from these two. Most AF pixel detections are common between the left and right image. The S7 contextual AF pixel detections (green) are removed as they will otherwise be counted twice. A and B illustrate the AF pixel positions which are detected by the absolute threshold test.

In addition, since at night signals from the SWIR2 channel (S6, 2.25 µm) should essentially be very close to zero over ambient temperature surfaces, but fires emit significantly at this wavelength (Figure 3) then where available the signal in this channel can be used to detect nighttime fires that might be missed by the tests based on fires signal in the MIR and TIR channel signals alone. This is especially the case since the pixel size of these SLSTR optical channels is 500 m, as opposed to

1 km for the thermal channels, so any fire will comprise a higher proportion of the S6 pixel area. An additional absolute threshold test is therefore used to make use of this capability.

$$L_{S6} > \mathrm{p1} + \overline{L}_{S6} + p2 \times n_{S6} \qquad \text{by night} \qquad (16c)$$

Where p1 = 0.05 and p2 = 2

Where L_{SWIR2} is the spectral radiance recorded in the S6 channel ($W \cdot m^{-2} \cdot sr^{-1} \cdot \mu m^{-1}$), p1 is the spectral radiance threshold set for S6 channel and *p2* a multiplier, $\overline{L}_{SWIR2}$ is the mean spectral radiance signal determined from the S6 channels at night over ambient cloud free land in the scene defined in Section 3.2, and n_{S6} is a measure of the S6 channel noise level (i.e. the median S6 signal in the scene). The definition of "night" here is $\theta_s < 90°$ (solar zenith angle), slightly higher than that used in the prior-stages of the algorithm to avoid issues associated with twilight.

Tests 17c is only implemented on nighttime observations, since during the daytime the high solar reflected signal at SWIR wavelengths swamp all but the largest/most extreme fire signals. Such fires would in any case be picked up by the MIR channel tests, and using the S6 channels by day would likely simply increase false alarm rate. Some nighttime fires however will be detected by the SWIR band tests whilst failing to be detected by the MWIR and LWIR based tests, because at night the SWIR bands are more sensitive to some smaller high temperature fires - due for example to the smaller pixel area of the measurements. Figure 11 shows an example of a nighttime case, where the S6 band identifies some fires (circled in green) that remain undetected by the S7 (MIR) -based tests, whilst also missing others that are detected by the S7 based tests (circled in red).

For those detections that are of vegetation fires rather than (the hotter) gas flares however, their FRP is still best retrieved with the MIR radiance method (i.e. using the S7 or F1 band data). This requires the MIR active fire pixel to be identified. However, as already stated there exist remaining spatial offsets between S7 and S6 even when the line and sample number of the S6 detected pixel is divided by two, so the same cluster based searching strategy detailed in Section 3.2.5 for the F1 and S7 channels is used here to identify the corresponding active fire cluster in the S7 channel that relates to the cluster detected in S6. This clustering is applied after the S6 line and sample number is divided by two in order to give a matching coordinate for the S7 pixel location.

Subject to further testing, we expect the F1_switch to be "ON" during routine processing. If the F1_switch is indeed set to "ON", all FRP values are calculated using the F1 radiances rather than the S7 radiances, and are reported at the F1 location of all detected AF pixels. If the F1_switch is "OFF" and all S7 data of the active fire considered unsaturated ($\leq S7_{AT}$), then the FRP of the fire is retrieved from S7. However if the F1_switch is "OFF" but the S7 brightness temperature of the active fire pixel exceeds the $S7_{AT}$ threshold beyond which it is considered inaccurate (currently expected to be 311 K), then the active fire pixels S7 spectral radiance cannot be used for FRP retrieval. At such pixels, it is still necessary to locate the F1 pixel corresponding to the S7 pixel – so that the F1 spectral radiance measure can be used instead of the S7. Furthermore, this use of F1 must be applied at all AF pixels in the fire cluster since the S7 and F1 pixels do not overlap precisely and have different sizes and degrees of oversampling that lead to strongly differing fire signals (see Figure 7). All AF pixels in a fire cluster must therefore have their FRP derived from either the S7 or F1 channels, rather than a mixture of both. The approach employed to do this is detailed in Section 3.2.5.

When using the corresponding S7 spectral radiance to retrieve FRP_{MIR} at an AF pixel detected by S6 (or when using F1 in the case of S7 pixels whose $T_{MIR} > S7_{AT}$ or the F1_switch is ON), the MIR background window spectral radiance required for FRP retrieval can be calculated using the surrounding pixels meeting the criteria set out in Equation 17a to 17e. The spectral radiance from the S7 (or F1) channel at the pixel location corresponding to the SWIR-based AF pixel detection, along with the mean and mean absolute deviation of the MIR signal at the surrounding pixel window, are then used in Equation 20 to calculate the MIR radiance derived FRP for the active fire pixel identified and detected in the S6 band.

For night-time detections over land, two FRP values are in fact provided in the final product. The first uses the MIR radiance method (Equation 19) and the S7 (or F1) signals recorded at each pixel in the AF cluster. The second uses the SWIR radiance method (Equation 20) and the S6 signals at each pixel in the AF cluster. The two methods of FRP derivation are provided because for vegetation fires the FRP retrieved using the MIR radiance method is more appropriate (Equation 20), but for gas flares (which are hotter than vegetation fires) the SWIR radiance method is more appropriate (Fisher and Wooster, 2018). The classification of detected AF hotspots into probable vegetation fires and probable gas flares is based on pre-set maps and included in the product output, so that users know on the basis of the detection location which FRP is most appropriate to use. In general, gas flaring mostly occurs in locations not particularly associated with vegetation fires (i.e. over the ocean or in arid desert regions). However, industrial gas flaring locations will change over time so a static map alone cannot provide a 100% accurate classification. Fortunately, the SWIR radiance method will tend to underestimate FRP at vegetation fires, whilst the MIR radiance method will tend to underestimate FRP at gas flares (Fisher and Wooster, 2018). Therefore, an alternative approach that the user can apply at night will be to select the highest FRP value from the two presented in the final product.

Since the pixel size of the S6 pixels is nominally 500 m, and since there remain spatial offsets between S6 and S7 channels, the data of the S6-detected AF pixels will be re-gridded using the aforementioned sampling (similar to a coordinate divide by two operation). If two or more S6 active fire pixels are found to lie within a single S7 pixel location when performing this calculation, then the total SWIR-radiance derived FRP derived for those pixels using their separate S6 radiances is summed to give a single S6-derived FRP value for the relevant S7 pixel location. After this, the cluster and search procedure of Section 3.2.5 is enacted to find the corresponding fire cluster detected in S7 to that detected in S6.

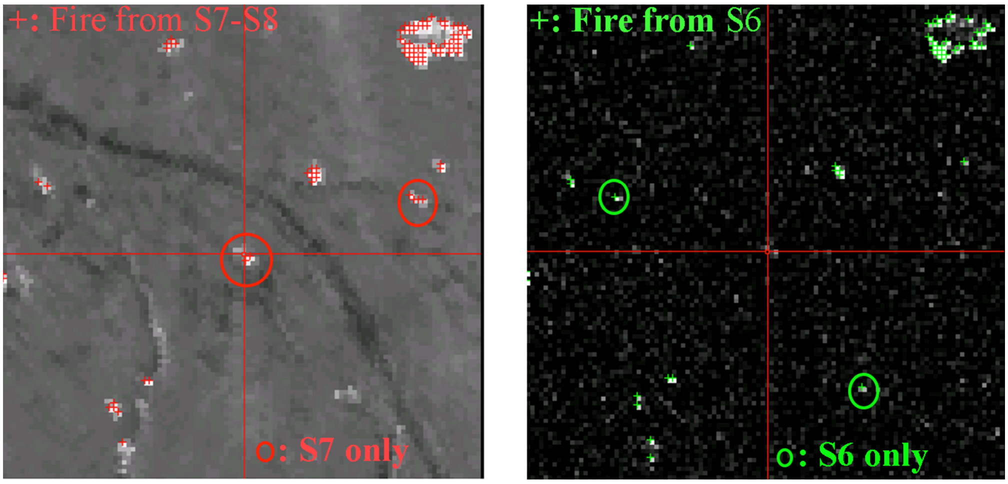

Figure 11. Night-time fires observed in the SLSTR S6 and S7 spectral bands. Red crosses show the AF pixels fire detected by the MIR-based contextual algorithm (based on S7 data), whilst green crosses denotes those detected using the SWIR-based thresholding method (based on S6 data). The background image on the left is in fact the brightness temperature difference between the S7 and S8 bands (which shows up AF pixels well), whilst that on the right is from the S6 band only. Note that most AF pixels in the scene are detected by both S7 and S6 active fire pixel detection approaches, but those circled in red at left are detected only by the S7 based

AF detection procedures, whilst those circled at right in green are those detected only by the S6-based AF detection procedures. For those AF pixels detected by the contextual algorithm based on S7 data, only the FRP value from S7/F1 will be given.

In most cases of nighttime fires, as shown in Figure 11, the active fire pixels will be detected by both the S6 thresholding (Test 16c) and the spatial contextual tests that are based mainly on S7. Both FRP derived from S6 and from F1 or S7 will be reported based on the S7 detection position, and the position of the same fire cluster identified using the S6 thresholding (Test 16c) will be removed. The S6 FRP will be redistributed to S7 fire pixel(s) in the same cluster based on their S7 FRP value since offset and different fire shape between S6 and S7. The identification of matching AF clusters should be based on the cluster search procedure detailed in Section 3.2.5 as mentioned above. Any additional active fire detections made using the S6 tests (but not detected in S7) will be kept however, and only the FRP value derived from the S6 radiances will be recorded and their position will be reported in S7 domain be divide by 2. Conversely though, any fires that are detected by the S7 tests but not S6 at night will only have S7 FRP values – since those fires are unlikely to be gas flares if they have not detected by S6 test.

Those active fire pixels detected with the F1 channel absolute thresholding tests (Test 16a and 16b), do not require background characterization values to be confirmed as fire pixels. However, the background characterization is still required to estimate the FRP of those fires (Equation 19), and its uncertainty. The S7 channel is usually better positioned to estimate the background MIR BT (as long as it is not saturated), as it has less noise and is not affected by the downscan anomaly issue that does affect F1 (low F1 BT values recorded after a high temperature pixel is scanned). In this case, the background characterization algorithm described in Section 3.2.2 is employed to characterise the MIR channel background statistics for those AF pixels detected using the F1 channel absolute threshold test. Note though that it is possible to have AF pixels detected by these absolute thresholding tests even when the MIR channel background characterization process fails. Where this occurs, the background window should continue to be expanded beyond 21 x 21 pixels to a maximum of 51 x 51 pixels until at least 50 background pixels are available to perform the background characterization process and thus provide the estimate of background window spectral radiance required to estimate FRP and its uncertainty. Since all active fire pixels detected by the absolute thresholding tests will by definition be very large fires, the fact that the background statistics in these cases will come from areas further away from the fire pixel than normal (and so maybe less representative of the fire pixel background itself) is less important than for lower FRP AF pixels, due to the very large MIR fire signals involved (i.e. in Equation 19; $L_{f,\,MIR} >> L_{b,MIR}$).

If even with the 51 × 51 pixel window upper limit, there remains insufficient background pixels to meet the 50 pixel criteria, which is expected to be a very rare occurrence, then the FRP should be estimated with $L_{b,MIR}$ taken as the median of the non-cloud, non-sunglint pixels of the sub-scene pixels having the same land/ocean classification as the fire pixel itself, and with the absolute uncertainty (δ_{L_b}) in the estimate of the fire pixel background radiance [used in Equation (19)] taken as that equivalent to a fixed uncertainty in the equivalent brightness temperature. Currently this value is set at 10 Kelvin (i.e. ±10 K uncertainty). The same absolute thresholding tests are used for land and ocean hotspots. For the equivalent S6 radiance derived FRP value (Eqn. 20) the background $L_{b,S6}$ value can be taken as the median of the S6 noise level.

3.2.4.2 Contextual Threshold Tests

For potential fire pixels from the set P_f corresponding to land hotspots and where the background characterization was successful but the potential fire pixel T_{S7} was not high enough to pass the absolute threshold test (16a or 16b), a series of contextual threshold tests are used to test confirmation of the potential fire pixel. These tests examine the T_{S7}, T_{S8} and $T_{S7\text{-}S8}$ potential fire pixel signals and compare these to the mean signals from the background window, with the exact thresholds adjusted to take into account the variability of the background window as measured by the mean absolute deviation. The contextual tests employed are:

$$L_{S7/S2} > \bar{L}_{S7/S2} \qquad (17a)$$

$$\Delta T_{S7-S8} > \Delta\bar{T}_{S7-S8} + p \times \sigma_{\Delta T_{S7-S8}} \qquad (17b)$$

Where p = 3.2

$$\Delta T_{S7-S8} > \Delta\bar{T}_{S7-S8} + p \qquad (17c)$$

Where p = 5.6 [Kelvin]

$$T_{S7} > \overline{T}_{S7} + p \times \sigma_{T_{S7}} \qquad (17d)$$

Where p = 3

$$T_{S8} > \overline{T}_{S8} + p \qquad (17e)$$

Where p = -4 [Kelvin]

These tests are based on those in Giglio *et al.* (2003), but adapted for SLSTR because of its wideband 3.7µm MIR channel, rather than the narrowband MODIS 3.9 um channel for which the tests were originally designed. Test (18a) has been added by day to help in the removal of potential fire pixels caused by sunglints, since at such pixels both S2 and S7 radiances will be increased whereas at fire pixels only the S7 will be.

Where $L_{S7/S2}$ is the ratio between the S7 band radiance and S2 band radiance of the potential fire pixel and $\overline{L}_{S7/S2}$ is the mean ratio between the S7 radiance and S2 radiance of the valid background pixels.

A daytime potential land fire pixel from P_f will be classified as a confirmed fire pixel if:

{The absolute threshold test (16a) is true}

or

{Tests (17a) – (17e) are true},

otherwise it is classified as a non-fire pixel.

A nighttime potential land fire pixel from P_f is classified as a true fire pixel if:

{The absolute threshold Test 16b is true; or Tests 16c is true}

or

{Tests (17b) – (17d) are true},

Otherwise it is classified as a non-fire pixel

At pixels for which the background characterization failed, i.e. due to an insufficient number of valid background pixels being identified in the background window, only Tests 16a to 16c can be applied. In this case if any of Tests 16a to 16c are true then the pixel is classified as a fire pixel, otherwise the pixel is classified as "unknown".

3.2.4.3 Gas flare / Volcano Classification

Gas flares and volcanoes can be discriminated by the detection algorithms presented here, since they also have high temperatures and thus can have high contrast with the surrounding background in the SLSTR MIR and SWIR bands. It is useful to identify when a detected AF hotpot is more likely to be due to either of these phenomena rather than a landscape fire, because applications of these data differ. A global map showing the location of gas flares and volcanoes is provided for this purpose.

The list of active volcano locations was generated from https://catalog.data.gov/dataset/global-volcano-locations-database, whilst that for the gas flares was from https://www.skytruth.org/viirs/. If a detected active fire pixel falls within a set distance of a location identified as a gas flare or active volcano (as specified within either of these two datasets), then it is classified as a suspected industrial hotspot or volcanic hotspot respectively (otherwise classed as a suspected landscape fire). Since the location of the gas flares and active volcanos is provided in world geodetic system latitude and longitude coordinates, Equation (19) is used to calculate the distance (d) in kilometers between the identified hotspot pixel and any active volcano or gas flare location:

$$d = a\cos(\sin(lat_f) * \sin(lat_c) + \cos(lat_f) * \cos(lat_c) * \cos(lon_f - lon_c)) * \mathrm{p} \qquad (18)$$

Where p = 6371 [km] and lat_f and lon_f are the latitude and longitude of the detected hotspot pixel, and lat_c and lon_c are the latitude and longitude of the volcano/gas flares.

Where *d* for a particular detected AF pixel is less than a preset value, currently assumed as 10 km, then the hotspot is given the relevant classification as probable volcano or probable gas flare, otherwise it is classed as probable vegetation fire. The classification is placed in the relevant flag file.

3.2.5 Fire Characterisation (Stage 5)

At each confirmed landscape vegetation fire pixel having a valid number of background pixels, the FRP is calculated as:

$$FRP_{MIR} = \frac{A_{sampl}}{10^6 \times \tau_{MIR}} \left(\frac{\sigma}{p}\right) \left(L_{MIR} - L_{b,MIR}\right) \qquad [\text{MW}] \qquad (19)$$

Where $p = 3.327\times10^{-9}$ [W·m^{-2} ·sr^{-1} ·µm^{-1} · K^{-4}]

Where A_{sampl} is the ground projection area of the sensor FOV (in m^2), which generally varies with viewing angle. Two look up tables (LUTs) stating the value of A_{sample} (m^2) to use in Equation 19 are provided for the two SLSRT nadir view MIR Bands (S7 and F1) in the auxiliary data files. These LUTs provide the value of A_{sample} according to the pixel index (0-1199) expressed in the original instrument domain (not the image domain). The indices file in the L1b data record is used to convert between the image domain and instrument domain pixel indices to select the correct A_{sample} value from the LUTs.

σ is the Stefan-Boltzmann constant (5.67x10^{-8} W.m^{-2}.K^{-4}), L_{MIR} is the spectral radiance of the fire pixel in the MIR channel (W·m^{-2}·sr^{-1}·µm^{-1}) and $\overline{L}_{MIR}$ is the mean spectral radiance of the valid background window pixels in the MIR channel (W·m^{-2}·sr^{-1} ·µm^{-1}), and *p* is the constant from the power-law linking radiance to 4th power of emitter temperature (W·m^{-2}·sr^{-1}·µm^{-1}· K^{-4} ; see Section 2.4.2). The actual value of *p* will depend on the exact spectral response function of the SLSTR MIR spectral band. The division by 10^6 converts the FRP into units of MW.

The value of atmospheric transmission in the MIR band (τ_{MIR}) will be taken from a further LUT that uses the total column water vapour (TCWV) and the pixel view zenith angle as inputs search criteria.

Importantly, clusters (i.e. spatially connected groups) of active fire pixels are much more common than isolated single active fire pixels (e.g. Figure 12a).

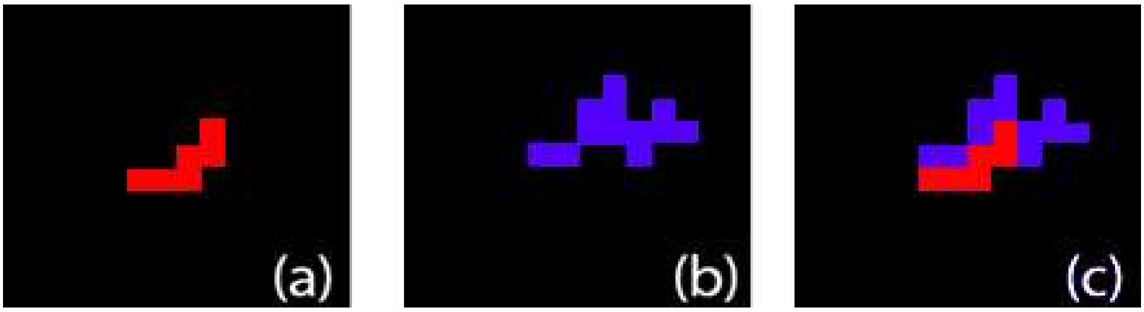

Figure 12. Example of an active fire (AF) pixel cluster. (a) AF pixel detections made using the MIR band (S7), where each AF pixel value still retains its BT_{MIR} value in the S7 band. (b) shows the AF pixel detection and clustering result using the alternative MIR band (F1) data. (c) The two sets of AF pixels overlain, showing their clearly different locations and cluster shapes.

The L_{MIR} value for an isolated or cluster-based active fire pixel for use in Equation (19) can only be read from S7 if that band has a BT_{MIR} value less than or equal to the S7 accuracy threshold (termed here $S7_{AT}$), currently taken as 311 K. For isolated AF pixels, or for AF pixels in clusters where all the AF pixels have a BT_{MIR} value lower than $S7_{AT}$, the L_{MIR} value for the AF pixel(s) can be derived from the S7 measurements.

However, for AF pixels where T_{S7} exceeds the $S7_{AT}$ threshold and less than absolute detection threshold (Test 16 a and b), the L_{MIR} values cannot be taken from S7 and values from F1 must be used instead. However, there are two issues associated with this:

1) Spatial mis-registration between S7 and F1 (even after ortho-geolocation) means that the location of an AF pixel identified in S7 cannot simply be taken as the same location in F1. Study of a limited number of ortho-geolocated Level 1b data show that whilst the F1 and S7 active fire pixels are geometrically quite well matched close to the centre point of the nadir view scan, they can have an increased offset further away from the nadir point. Thus, whilst the F1 AF pixel

locations matching S7 will certainly be close to the S7 AF pixel locations, their exact locations must be newly identified.

2) Differences in the shape and size of the S7 and F1 pixels mean that a cluster of AF pixels need to have their 'fire cluster' FRP retrieved from either S7 or F1, and not a mixture of both. Thus if even a single S7 pixel in a cluster has an T_{S7} exceeding the $S7_{AT}$ threshold, all pixels in the cluster must have their FRP estimated using L_{MIR} values derived from F1.

There are two situations envisaged:

Situation 1 (common at night):

AF pixels whose T_{S7} exceeds the $S7_{AT}$ threshold and less than absolute threshold, but which have values below this threshold at every one of their valid background window pixels.

In this case the Stage 2 background characterisation results taken from within the AF pixel's background window (Section 3.2.2) can still be used in the AF characterisation process - and specifically the mean and mean absolute deviation of the qualifying background window pixels in both the MIR (S7) and LWIR (S8) bands.

The AF pixels still have to be identified in the F1 band however because one or more of them in the cluster exceeds the $S7_{AT}$ threshold. The approach to identify them employs a pixel clustering algorithm and an AF pixel detection approach that uses only the F1 channel. The approach is expressed via the eight stages detailed below:

i) Cluster the S7 band AF fire pixels into individual clusters. This can be done using "connected-component labelling", an approach used in computer vision to identify connected regions in imagery (e.g. https://en.wikipedia.org/wiki/Connected-component_labeling). The method groups a spatially connected set of AF pixels into a single cluster, based on a series of Steps.

Step 1: The AF detections made in S7 are used to create a binary image "mask" that has.

V={1} where a pixel is an AF pixel
V={0} where a pixel is not an AF pixel.

Step 2: Starting from the first pixel in the binary image mask. Set a current label (C) counter to 1.

Step 3: If this pixel is an AF fire pixel [i.e. has V={1}] and it is not already labelled with the current label value then give it the current label (C) and add it as the first element in a queue, then go to Step 4. However, if this pixel is not an AF pixel [i.e. has V={0}] or it is already labelled, then repeat Step 2 for the next pixel in the binary mask.

Step 4: Pop out an element from the queue, and look at each of its neighbours in the binary image mask (based on any type of connectivity [up, down, left, right or diagonal]. For each neighbour that is itself an AF pixel (and which is not already labelled), give it the current label and add it to the queue. Repeat Step 4 until there are no more elements in the queue.

Step 5: Goto Step 3 for the next pixel in the binary image mask and increment current label (C) by 1.

Each AF cluster now has its individual AF pixels coded with a different label value, one for each cluster. The size of each cluster in samples and lines (F_x, F_y) should be recorded from the maximum and minimum sample and line positions of the AF pixels making up the relevant cluster, and the total number of AF pixels making up each cluster (N_f) is also stored, along with the number of AF pixels in the cluster having $T_{S7} > S7_{AT}$ (N_s).

ii) Using Equation (20), calculate the FRP of those AF pixels in the cluster that have $T_{S7} \leq S7_{AT}$, and store the total of this as FRP_{S7}. The mean and mean absolute deviation of the qualifying background window pixels in S7 are also be carried forward to the next step.

iii) Centre at the top left AF pixel in the cluster having $T_{S7} > S7_{AT}$ and select a window of size (F_x + 10) samples and (F_y + 10) lines around that location in the F1 band. This window will be used to identify the corresponding AF fire pixels of the cluster in the F1 band. All F1 pixels within this window are checked to determine whether they are an AF pixel or not using what we term the "F1 contextual detection" method, based on their F1 signals and the average of all mean and mean absolute deviation of the S7 background window pixels that were identified for this particular S7 AF pixel cluster. The tests used are:

During daytime:

{The absolute threshold test (16a) is true}

or

{if the $\sigma'_{T_{S7}}$ (average of all mean absolute deviation of the S7 background window) >= 1 then:

$$T_{F1} > \overline{T}'_{S7} + p_1 \times \sigma'_{T_{S7}}$$

else

$$T_{F1} > \overline{T}'_{S7} + \sigma'_{T_{S7}} + p_2 \}$$

Where $\overline{T}'_{S7}$ is the mean of all mean S7 pixel signals in the background window, p1=3 and p2=2 Kelvin.

During nighttime:

{The absolute threshold Test 16b is true}

or

{if the $\sigma'_{T_{S7}}$ >= 1 then:

$$T_{F1} > \overline{T}'_{S7} + p_1 \times \sigma'_{T_{S7}}$$

else

$$T_{F1} > \overline{T}'_{S7} + \sigma'_{T_{S7}} + p_2 \}$$

Where p1=3 and p2=2 Kelvin.

iv) Once the AF pixels have been identified in the F1 band, cluster these using the same Connected-component_labeling approach as in (i) above.

v) Identify the F1 cluster that matches the detected S7 cluster. In Figure 12c for example, the blue coloured AF fire cluster detected in F1 should be identified as the same cluster as the red coloured cluster detected in S7. The same Connected-component_labeling as in (i) can be used to identify whether the two clusters are connected. If they are connected, then the blue F1 fire cluster will be regarded as the corresponding fire cluster to that shown in red in S7.

vi) Assuming that the total FRP for a fire cluster should be the same whether it is measured in F1 or in S7, use the F1-derived FRP values to calculate the FRP when the F1_switch is on, and report F1 location for all the AF pixels. If the F1_switch is OFF, for pixels where $T_{S7} > S7_{AT}$, the FRP is retrieved from F1 in the case where a cluster contains S7 pixels with $T_{S7} > S7_{AT}$, but the FRP is redistributed back to the matching S7 clusters AF pixel locations in order to ultimately have all FRP records corresponding always to AF pixel locations detected in S7 (and not F1). To accomplish this, the total FRP of the cluster is calculated from the clusters F1 AF pixels using Equation 19 (and the background window parameters measured in S7) and recorded as FRP_{F1}.

vii) If the F1_switch in on, the FRP recorded as FRP_{F1} for an F1 detected cluster, and the location of fire pixels are reported in F1 domain. If F1_switch is off, then the FRP_{F1} need to be distributed around the S7-deteced AF pixels of the matching S7 cluster. First, in the S7 cluster AF pixels with $T_{S7} \leq S7_{AT}$ have their FRP coded as that derived earlier using the S7 band data. The FRP total of these pixels is termed FRP_{S7}. Then, the remaining S7 pixels that have $T_{S7} > S7_{AT}$ are given the FRP value $(FRP_{F1}- FRP_{S7})/N_s$. The total FRP of the cluster in S7 will therefore be the same as recoded in the matching F1 cluster.

The approach is illustrated in Figure 12, assuming that the AF pixels are detected on S7 and F1 as shown in Figure 12a and 12b respectively using the methods outlined above. The corresponding S7 and F1 AF clusters partly but not wholly overlay, as showin in Figure 12c, due to the differing pixel sizes and shapes and the spatial offset between the S7 and F1 spectral bands. The total FRP of the AF cluster detected in F1 is calculated (as FRP_{F1}), then the total FRP for those AF pixels detected in the matching S7 cluster that have $T_{S7} \leq S7_{AT}$ (FRP_{S7}) is subtracted from this value. The result of this calculation is divided by the number of S7 cluster AF pixels having $T_{S7} > S7_{AT}$ (N_s) and the final value stored as the FRP for each of the N_s pixels whose $T_{S7} > S7_{AT}$. In this way, all the AF pixels detected in the S7 cluster have a valid FRP value, and the total FRP recoded for them is equal to FRP_{F1}. For example, in Figure 12a there are six AF pixels identified in S7, and two of these have an $T_{S7} > S7_{AT}$ which means their FRP cannot be accurately calculated from their S7 signals. The remaining four S7 pixels have $T_{S7} \leq S7_{AT}$ and thus can have their FRP accurately calculated from their S7 signals. Lets assume the total FRP of these four pixels recorded in S7 (i.e. FRP_{S7}) is 40 MW. Now the corresponding fire cluster detected in F1 (Figure 12b) has twelve AF pixels within it, and lets say that these have a total FRP of 300 MW as calculated via their F1 signals (i.e. FRP_{F1}). In the final FRP output, at the location of the two S7 pixels having $T_{S7} > S7_{AT}$ the FRP is recorded as (300 – 40) / 2 = 130 MW each.

viii) The FRP uncertainty value for the cluster is calculated using Equation (22) along with the AF pixel spectral radiances from F1, whilst the background window values are still coming from S7.

When the F1 switch is ON, the approach for retrieval the FRP value for each fire is very similar to eight stage descripted in situation 1 except minor changes as following:

i) Cluster the S7 band AF fire pixels into individual clusters.

ii) We do not need the FRP value from S7 detection as all the FRP and fire pixel position will be reported in F1 domain. However, the mean and mean absolute deviation of the qualifying background window pixels in S7 for all the pixels in the fire cluster are carried forward to the next step.

iii) Centre at the top left AF pixel in the cluster, notice this does not have to be the top lest pixel having a $T_{S7} > S7_{AT}$, and select a window of size (Fx + 10) samples and (Fy + 10) lines around that location in the F1 band. This window will be used to identify the corresponding AF fire pixels of the cluster in the F1 band. The equation to detect the fire will be the same in situation 1.

iv) Once the AF pixels have been identified in the F1 band, cluster these using the same Connected-component_labeling approach as in (i) above.

v) Identify the F1 cluster that matches the detected S7 cluster. In Figure 12c for example, the blue coloured AF fire cluster detected in F1 should be identified as the same cluster as the red coloured cluster detected in S7. The same Connected-component_labeling as in (i) can be used to identify whether the two clusters are connected. If they are connected, then the blue F1 fire cluster will be regarded as the corresponding fire cluster to that shown in red in S7.

vi) Assuming that the total FRP for a fire cluster should be the same whether it is measured in F1 or in S7, use the F1-derived FRP values to calculate the FRP using Equation (19).

vii) The FRP recorded as FRPF1 for an F1 detected cluster, and the location of fire pixels are reported in F1 domain. The corresponding S7 cluster will be discarded as all the location and FRP for the fire cluster are reported in F1 domain already.

viii) The FRP uncertainty value for the cluster is calculated using Equation (22) along with the AF pixel spectral radiances from F1, whilst the background window values are still come from S7. If a corresponding F1 fire cluster can not be found through this approach, the fire position and FRP will be report in S7 domain

Situation 2 (uncommon at night):

For AF pixels having $T_{S7} > S7_{AT}$ when measured in the S7 channel, and for which their background window also contains pixels having $T_{S7} > S7_{AT}$ in the same channel, the background window characterisation of Stage 2 needs to be conducted using F1 data in place of S7 data. This is the "non-classic" situation not routinely encountered with sensors such as MODIS or SEVIRI, but which is encounted with SLSTR due to the comparatively low saturation of its standard "S7" band. An future algorithm evolution will entail the AF detection and characterisation process to proceed in this "non-classic' case.

For most active fire pixels detected at night, two FRP values are given, as introduced in Section 3.2.3.1. The two values come from application of the MIR and SWIR radiance methods of FRP derivation, and we term them FRP_{MIR} and FRP_{SWIR} respectively. Users will be recommended to use FRP_{SWIR} for suspected gas flares and FRP_{MIR} for suspected vegetation fires. Classification of the detected hotspot pixels into these two classes is provided in the product, based on pre-recorded maps. Active volcanoes are also detected by the algorithm, and present a very wide range of temperatures, including below the minimum threshold for accurate application of the FRP_{SWIR} and FRP_{MIR} methods. Thus, whilst these FRP metrics will be useful in assessing thermal changes at active volcanoes, they are unlikely to provide unbiased estimates of active volcano radiative power output.

As introduced in Section 3.2.3.1, the users will also be able to compare FRP_{MIR} and FRP_{SWIR} and in general the higher value will be the most appropriate for the AF hotspot. Therefore users can select to override the hotspot classification and use the higher of the two FRP values if they wish.

The MIR radiance FRP (appropriate for gas flares) is calculated with Equation (20). The SWIR radiance FRP (appropriate for gas flares) is calculated with Equation (21) and the SWIR band (S6) spectral radiance signal:

$$FRP_{SWIR} = \frac{A_{sampl}}{10^6 \times \tau_{SWIR}} \left(\frac{\sigma}{p} \right) \left(L_{SWIR} - L_{b,SWIR} \right) \tag{20}$$

Where p is the S6 equivalent of the factor used in (20) [$W \cdot m^{-2} \cdot sr^{-1} \cdot \mu m^{-1} \cdot K^{-4}$]. This is currently calculated at 6.1 x 10^{-9} $W \cdot m^{-2} \cdot sr^{-1} \cdot \mu m^{-1} \cdot K^{-4}$. $L_{b,SWIR}$ is median of the instrument noise at night (which can be calculated from the sub-scene and is expected to usually be of the order of 0.015 $W \cdot m^{-2} \cdot sr^{-1} \cdot \mu m^{-1}$).

Where A_{sampl} is the ground projection area of the sensor FOV (in m^2), which generally varies with viewing angle. A look up table (LUT) stating the value of A_{sample} (m^2) to use in Equation 21 will be provided for the SLSTR nadir view S6 band in the auxiliary data files, and this will provide the value of A_{sample} according to the pixel index (0-2399) expressed in the original instrument domain (not the image domain). The indices file in the L1b data record is used to convert between the image domain and instrument domain pixel indices to select the correct A_{sample} value from the LUTs. The value of atmospheric transmission in the SWIR2 band (τ_{SWIR}) will be taken from a further LUT that uses the total column water vapour (TCWV) and the pixel view zenith angle.

3.2.6 Atmosphere transmittance

Wooster et al. (2015) demonstrate that the primary atmospheric effect of significance with regard to FRP derivation is the non-unitary atmospheric transmittance (T) in the MIR atmospheric window. The impact of upwelling atmospheric path radiance and reflected downwelling atmospheric radiance can be neglected due to their similarity at the fire pixel and surrounding background pixels.

Values of transmittance have been pre-computed as a function of the total column water vapour (TCWV). For each value of TCWV, the mean transmittance has been estimated for varying CO_2 concentrations of 380 to 420 ppmv, aerosol optical thicknesses between 0.2 and 1.0 for various aerosol types, different atmospheric vertical profiles and surface brightness temperatures. The ozone concentration was set to 354 DU. The transmittance T is estimated with the following expression as a function of the satellite viewing angle θ_v

$$T = \exp\left(\frac{-\tau}{\cos(A + Bq\theta_v + C(q\theta_v)^2)}\right) \quad (21)$$

with $q = \pi / 180$. Values of A, B and C have been adjusted to fit exactly the variations of τ estimated with Equation (21) as a function of θ_v.These tabulated values are given in a look up table in Section (A.1). The transmittance is linearly interpolated from this LUT according to the actual water vapour concentration U_{H2o}.

3.2.7 Uncertainty Budget

FRP Uncertainty Estimation and Fire Pixel Confidence Assessment (Stage 6) are described in this section.

3.2.7.1 FRP Uncertainty Estimation

The estimation of FRP via the MIR and SWIR radiance methods of Equation (19) and (20) are subject to random errors resulting from uncertainties in the value of a and τ and in the assessment of Lf and Lb. Assuming that these are uncorrelated, the corresponding uncertainty (δ_{FRP} ; MW) in FRP is:

$$\delta_{FRP} = FRP\sqrt{\left(\frac{\delta_a}{a}\right)^2 + \left(\frac{\delta_T}{T}\right)^2 + \left(\frac{\delta_{L_{MIR}}}{L_{MIR} - L_{b,MIR}}\right)^2 + \left(\frac{\delta_{L_{b,MIR}}}{L_{MIR} - L_{b,MIR}}\right)^2} \qquad (22a)$$

Where δ_a is the absolute error (in MW) resulting from the power law approximation to the Planck function used in deriving Equation (20) and (21). Assuming a fire temperature range of 675 to 1300K the value of $\frac{\delta_a}{a}$ is about 0.1 at one sigma (Wooster et al., 2005)

δ_τ is the absolute error in the estimation of atmospheric transmission in the channel used for FRP derivation: (i) the uncertainty on the actual atmospheric vertical composition except the water vapour concentration and (ii): the atmospheric correction error resulting from the uncertainty on the water vapour concentration. This total error writes:

$$\delta_t = \sqrt{\delta_b^2 + \delta_{H_2O}^2} \qquad (22b)$$

The former error is

$$\sigma_b = 10^{-5}\tau \\ (816.1 - 27.5\theta_v + 2.3\theta_v^2 - 0.0585\theta_v^3 + 0.0005\theta_v^4) \qquad (22c)$$

and the latter

$$\sigma_{H_2O} = \frac{\partial \tau}{\partial U_{H_2O}} \sigma_{U_{H_2O}} \qquad (22d)$$

with

$$\sigma_{_{H_2O}} = 0.24287 + 0.11172 U_{H_2O} - 0.00090 U_{H_2O}^2 \quad (22e)$$

Equation (22e) holds for the total column water vapour field delivered by ECMWF.

$\delta_{L_{MIR}}$ represents the absolute radiometric error resulting from the combination of: (i) the radiometric noise (σ_n) of the SLSTR MIR channel, (ii) the random errors (ϵ_{b1}) related to the Level 1b processing effects and finally (iii) the instrument saturation above 500K. For this latter effect, the error term $(\sigma_{\tilde{I}_s})$ corresponds to the uncertainty on the estimation of the radiance $\tilde{I}_s$ that would have been observed if SLSTR were not subject to saturation. Systematic errors such as calibration uncertainty are not included in this term. This error is

$$\sigma_{L_f} = \sqrt{(\sigma_n)^2 + (\tilde{I}\epsilon_{b1})^2 + (\sigma_{\tilde{I}_s})^2} \qquad (22f)$$

The value of σ_n is taken from the level 1b product, it set as 0.01 at present. $\tilde{I}\epsilon_{b1}$ represents the fractional uncertainty induced by the image processing chain used to deliver the version of the SLSTR data input into the algorithm. At present this is considered negligible.

$\sigma_{\tilde{I}_s}$ is the error associated with the saturated pixel default radiance value. This term is non-zero only over saturated F1 pixels, which with SLSTR are expected to be extremely rare as F1 can measure BT as high as 450 or 500K (depending on the specific SLSTR instrument, as each are slightly different). $\sigma_{\bar{I}_s}$ is set at 0.05 over saturated F1 pixels and 0 elsewhere.

$\delta_{L_{b,MIR}}$ is the atmospherically corrected standard deviation of the background radiance .

3.2.7.2 Fire Pixel Confidence Assessment

Fire pixel errors of omission and commission are always present in the results of any active fire detection algorithm. There is an inherent trade off as it is possible to reduce errors of commission (i.e. false alarms) to zero by having an extremely conservative fire detection algorithm with very strict thresholds. The downside of this approach is that errors of omission will be very high – and many and perhaps most true active fire pixels may fail to be detected. In the SLSTR algorithm we have instead attempted to minimise the occurrence of false alarms via an optimised contextual fire detection scheme whose principles are based on forerunner algorithms that have shown strong levels of performance levels when applied to MODIS polar orbiting and SEVIRI geostationary datasets. Nevertheless, errors of commission with these prior schemes are noted to be of the order of 5 to 10%, and so a similar commission error is expected with SLSTR, certainly until more experience is gained with the data and the algorithm can be tuned or modified accordingly. This is especially true since we currently do not know the performance level of the cloud detection scheme upon which the fire detection algorithm depends.

Since errors of commission are certainly going to be present in the output dataset, a measure of detection confidence for each confirmed fire pixel is ideally required, such that users can opt to utilise only certain high confidence active fire detections for example. The scheme for deriving the confidence measure is based on the approach of Giglio *et al.* (2003), and which has also been adopted for the SEVIRI FRP product (Wooster and Roberts, 2008). Detection confidence is defined according to a combination of the absolute and relative fire-pixel signal, and to the number of near-neighbouring cloud and water pixels (the idea here being that fire pixels detected close to such features are more likely to be false detections due to sunglint or other non-fire effects (e.g. a strong thermal contrast across a geographic boundary; coupled with interchannel spatial misregistration between the TIR and MIR bands). The confidence measure employs T_{MIR}, N_w, N_c, and the standardized variables Z_{MIR} and $Z_{\Delta T_{MIR-TIR}}$, which are defined as:

$$Z_{MIR} = \frac{T_{MIR} - \overline{T}_{MIR}}{\sigma_{MIR}} \quad (23)$$

$$Z_{\Delta T_{MIR-TIR}} = \frac{\Delta T_{MIR-TIR} - \Delta \overline{T}_{MIR-TIR}}{\sigma_{\Delta T_{MIR-TIR}}} \tag{24}$$

T_{MIR} comes from either the S7 or F1 bands, whereas T_{TIR} comes always from S8.

These quantities represent the number of absolute deviations that T_{MIR} and $\Delta T_{MIR-TIR}$ lie above the background, and are analogous to the more commonly used Z-scores that are calculated using the standard deviation. A ramp function is defined as:

$$S(\chi;\alpha,\beta) = \begin{cases} 0; & \chi \le \alpha \\ (\chi-\alpha)/(\chi-\beta); & \alpha < \chi < \beta \\ 1; & \chi \ge \beta \end{cases} \tag{25}$$

The confidence assigned to each fire pixel is composed of a combination of five sub-confidences, labelled C1 to C5, each having a range of 0 (lowest confidence) to 1 (highest confidence). For daytime fire pixels, these are defined as

$$C_1 = S(T_{MIR};310K,340K) \tag{26a}$$

$$C_2 = S(Z_{MIR};2.5,6) \tag{26b}$$

$$C_3 = S(Z_{\Delta T_{MIR-TIR}};3,6) \tag{26c}$$

$$C_4 = 1 - S(N_c;0,6) \tag{26d}$$

$$C_5 = 1 - S(N_w;0,6) \tag{26e}$$

For C_1, 310 K represents a brightness temperature that is likely to be towards the minimum brightness temperature required for a pixel to be considered a fire pixel (and is thus less obviously a fire), while based on experience, 340 K represents a typical value for a reasonably obvious fire. For C_2, $Z_{MIR} = 2.5$ is the minimum value required of fire pixels by the detection algorithm, whereas $Z_{MIR} = 6$ represents a typical value (again based on experience) for an unambiguous fire. A similar rationale applies to the definition of C_3. C_4 reduces the detection confidence as the number of adjacent cloud pixels increases, accounting for the fact that fire pixels detected along cloud edges are more likely to suffer from cloud contamination, potentially triggering a false alarm via reflected sunlight. Finally, C5 reduces the confidence as the number of adjacent water pixels increases, reflecting the greater likelihood that the detected fire pixel is instead a false alarm induced by a coastal boundary.

Following Giglio *et al.* (2003), the detection confidence of the fire pixel C is then defined as the geometric mean of the sub confidences, i.e.

$$C = \sqrt[5]{C_1 C_2 C_3 C_4 C_5} \tag{26f}$$

For night-time fire pixels, the thresholds of C_1 are altered so that

$$C_1 = S(T_{MIR}; 305K, 320K) \tag{26a'}$$

The others remain the same as for daytime imagery.

In the case where a fire pixel has been detected with an absolute threshold test, the fire confidence parameter C is automatically set to 1 since these are assumed definitely to be fires due to their strong contrast with the background. Thus the confidence value of the fire pixels detected with the SWIR2 (S6) band (Equation 14c) will be 1.

3.3 Oceanic and Coastal hotspots

Whilst the pre-launch active fire detection and FRP retrieval algorithm of Wooster *et al.* (2012) was designed only to detect and characterize hotspots on the land surface, the detection of gas flares in coastal and oceanic regions is desirable. The following adaptations are used for this task at daytime, along with an adapted land/ocean mask used to identify the location of oceanic and coastal locations to search within. By night over the ocean the absolute threshold Test 16c that uses S6 is deployed to detect the gas flares. Since these are definitely not active vegetation fires, their FRP only needs to be reported as that derived from S6. Thus, the location of the S6 derived FRP can simply be given on the S7 image grid by dividing their S6 location column and row value by a factor of two (since S6 has a 500 m nominal pixel size compared to 1000 m in S7).

3.3.1 Stage 1a

Similar to Stage 1a for the land hotspots, the task of Stage 1a here is to highlight potential hotspots (i.e. gas flares) in ocean areas. However, since the potential geographic area for flares to occur in is relatively small, and the oceanic background is much more homogeneous than the land, the region is not subdivided as it was for the land hotspot detection Stage 1a. Firstly, the number of cloud free pixels within the geographic ocean mask window specifying the region to search within is calculated (N_{cf_ocean}). If this is greater than a pre-determined threshold (currently set at 2000 pixels) the scene will be treated as valid for potential gas flare detection and will be processed for Stage 1a.

In this case the mean values of T_{MIR}, T_{TIR}, and $\Delta T_{MIR-TIR}$ for all cloud-free ocean pixels in the region are used as the respective spectral filter thresholds ($\overline{T}^{cf}_{MIR}$, $\overline{T}^{cf}_{TIR}$, $\overline{\Delta T}^{cf}_{TIR-MIR}$), against which each cloud-free ocean pixel in the region are tested for inclusion into the potential fire pixel set P_2 relevant to the potential ocean hotspot area.

If N_{cf_ocean} is too low to meet the pre-determined threshold criteria specified above, then default thresholds are used:

By day:

$T_{S7} > p$ (11d' where ' indicates a variation on the original test 11d)

Where p = 295 [Kelvin]

and

$\Delta T_{S7-S8} > p$ (11e')

Where p = 1 [Kelvin]

Pixels failing these preliminary tests are immediately classified as non-hotspot pixels. Pixels passing these tests belong to set P_1 relating to the potential ocean hotspot area.

3.3.2 Stage 1b

A similar approach is used for ocean areas as for the land areas, though again instead of using subscenes, the entire potential ocean hotspot area within the scene is used at once. The edge detection filter is applied to the potential ocean hotspot area, and pixels passing the test are those where the filter output (h_K) exceeds a threshold defined in relation to the filter output standard deviation calculated from all the clear sky, ocean pixels in the potential ocean hotspot area (as specified by Equation 11). In the case where there is an insufficient number of pixels (currently < 2000) in the potential ocean hotspot area for the proper determination of σ_{fK} for a particular hotspot pixel (which is expected to be a rare occurrence), default values of 1 for σ_{fK} are used instead. As with other absolute thresholds used herein, these maybe adapted as more experience of SLSTR observations made under different conditions is gained over time.

3.3.3 Stage 2

Similar to the land, at each potential fire pixel belonging to set P_f relevant to the ocean areas, b_W is initially set as 5. The center pixel of this 5 × 5 window is the potential fire pixel itself, and so is discounted from the background window, and the immediately surrounding eight background pixels are also discounted since their closeness to the potential fire pixel can result in their radiances being contaminated by the fire radiance itself. Thus for the 5 × 5 pixel window, a total of 16 pixels are initially included as potentially valid pixels for use in the background characterisation. From these 16 pixels, the set of valid background pixels P_b are selected based on their being identified as clear-sky, ocean pixels that for daytime observations are not influenced by strong sun glint, and which should pass the following tests in addition to Tests 13a,13b and 13 e :

$$\Delta T_{S7\text{-}S8,w} < p \qquad (13d')$$

Where p = 10 [Kelvin]

In the same way as for the land hotspot tests, if at least 25% of the background window pixels (which are $b_W \times b_W$ in number) are deemed valid, and their absolute number is 8 or more, then the background window statistical characterization process proceeds immediately using a window size b_W of 5. If either of these conditions are not met, the window size b_W is increased through 7, 9, 11, 13, 15, 17, 19 and 21 until the criteria is met, as for the land hotspot case.

Following Giglio *et al.* (2003) the number of valid background pixels within the background window is recoded as N_b. The number of pixels excluded from the background window is also recorded for use in false alarm reduction, and in defining the fire pixel confidence measure. The number of pixels (N_f) excluded as being "background fires" is set as the total number failing test 13c' and test 13d', The number excluded as being land pixels or cloud-contaminated pixels is recorded as $N_{w/l}$ and N_c respectively.

For each potential fire pixel where a sufficient number of valid background pixels are identified (which is the vast majority of cases), the background characterisation is classed as successful and a number statistical measures computed from the valid background pixel set P_b relating to the potential ocean hotspot area. These are $\overline{T}_{S7}$ and σT_{S7}, the respective mean and mean absolute deviation of T_{S7} ; $\overline{T}_{S8}$ and σ_{S8}, the respective mean and mean absolute deviation of T_{S8} ; $\overline{\Delta T}_{S7-S8}$ and $\sigma_{\Delta T_{S7-S8}}$, the respective mean and mean absolute deviation of ΔT_{S7-S8}, $\overline{\rho}_{S2}$ and $\sigma\rho_{S2}$, the mean and mean absolute deviation of ρ_{S2} (Band S2).

3.3.4 Stage 3

For potential fire pixels from the set P_f corresponding to ocean hotspots, but where the background characterization was successful but the potential fire pixel brightness temperature (T_{S7}) was not high enough to pass the absolute threshold Tests 16a to 16c, a series of contextual threshold tests are used to test the potential fire pixel and confirm whether it is indeed a true fire pixel.

In addition to the unaltered Test 17a, slightly lowered thresholds are used with the ocean equivalents for Tests 17b to 17f (termed for the ocean Tests 17b' to 17f'). This is possible due to the oceanic background being considerably more uniform than the land surface, and is necessary due to the typically relatively small increases in the thermal signals representative of gas offshore flares.

$$L_{S7/S2} > \overline{L}_{S7/S2} \tag{17a'}$$

$$\Delta T_{S7-S8} > \Delta \overline{T}_{S7-S8} + p \times \sigma_{\Delta T_{S7-S8}} \quad \text{(17b')}$$

Where p = 2

$$\Delta T_{S7-S8} > \Delta \overline{T}_{S7-S8} + p \quad \text{(17c')}$$

Where p =2.5 [Kelvin]

$$T_{S7} > \overline{T}_{S7} + p \times \sigma_{T_{S7}} \quad \text{(17d')}$$

Where p = 2

$$T_{S8} > \overline{T}_{S8} + p \quad \text{(17e')}$$

Where p = -2 [Kelvin]

A daytime potential oceanic fire pixel from the set P_f will be classified as a confirmed fire pixel if:

{The absolute threshold Test (16a) is true}

or

{Tests (17a') – (17e') are true},

otherwise it is classified as a non-fire pixel.

At potential oceanic fire pixels from the set P_f where the background characterization failed, i.e. due to an insufficient number of valid background pixels being identified in the background window, the pixel is classified as "unknown".

3.3.5 Stage 4 FRP Retrieval

The FRP of ocean hotspots are calculated with Equation 21 since they are all assumed to be gas flares and thus it is relevant to have their FRP calculated using the SWIR radiance method, and their confidence is retrieved using Equation 28 (Section 3.2.6.2).

However, there is some offset between S7 and S6, so the same strategy detailed in Section 3.2.5 used to identify matching fire clusters in F1 and S7 is used here to find the corresponding fire cluster on S7 as has been identified in S6. The total FRP from the S6 calculation is then redistributed equally to the corresponding location of the S7 "gas flare" pixels by dividing the total FRP measured in the SWIR band S6 by the total number of active fire pixels in S7 identified in the corresponding AF cluster.

4 PRACTICAL CONSIDERATIONS

4.1 Cloud masking

Cloud masking is essential to an active fire product, due to the fact that optically thick clouds make it impossible to identify active fires through passive remote sensing, and solar reflected MIR radiation from certain clouds can appear similar to fire signals. Thus, some cloud-contaminated pixels will likely be falsely classified as fires if they are not masked out prior to active fire detection.

However, it is also the case that some cloud masking algorithms use tests (e.g. those based on thermal channel differences) that can erroneously identify fire-related hotspot pixels as cloud. Furthermore, some cloud mask algorithms also identify optically thick smoke as cloud, even though fire detections can typically be made through smoke since it is relatively transparent at MIR wavelengths (unlike meteorological cloud). Therefore care should be taken in the deployment of the generic SLSTR cloud mask with regard to its use in masking the SLSTR observations prior to Stage 1 of the fire detection algorithm (Figure 6), and it is possible that only some of the cloud masking tests will be relevant to masking data prior to application of the fire detection and characterization algorithm.

To try to ensure that the cloud mask available for SLSTR is of maximum relevance to the fire product, over the land it can potentially be enhanced or even replaced by a further simple mask developed for the fire product based on the following simple tests taken from Giglio *et al.* (2003b):

For daytime

$\{(\rho_{RED} + \rho_{NIR} > 0.9)$ or $T_{TIR} < 265$ K$\}$

or

$\{ (\rho_{RED} + \rho_{NIR} > 0.7)$ and $T_{TIR} < 285$ K$\}$
$\{ (abs(T_{MIR} - T_{TIR}) > 4)$ and $T_{TIR} < 273$ K$\}$
For nighttime

$\{ T_{TIR} < 273$ K$\}$

The same tests, possibly with adjusted thresholds, can also be applied over oceanic areas.

4.2 Water masking

Given the contextual nature of the AF detection algorithm, when analyzing potential land AF pixels it is important to accurately exclude water and mixed land-water pixels during the background characterization stage. Such pixels are usually cooler than adjacent land pixels during the day. Unknowingly including water and mixed land-water pixels in the background window can cause false alarms due to altered brightness temperature signals. Also contributing to this phenomenon is the fact that compared to land, water pixels frequently have lower values of $\Delta T_{MIR-TIR}$ due to more similar spectral emissivity's than land. Water and mixed land-water pixels contaminating the background window can therefore decrease $\Delta\overline{T}_{MIR-TIR}$ and thus increase the likelihood that a false alarm AF detection will occur. Therefore prior to the AF detection algorithm being applied, a set of tests is used in daytime areas to identify any additional water contaminated pixels that have not been masked out by the land-water mask. Following Giglio *et al.* (2003), we use a simple test based on the 0.86 µm and 2.1µm reflectance (ρ) values, and the Normalized

Difference Vegetation Index (NDVI) of the valid background pixels, where NDVI=(ρ_{NIR}-ρ_{RED})/(ρ_{NIR} + ρ_{RED}). This particular combination was chosen to reduce the likelihood of confusing cloud shadows and burn scars, which also have low surface reflectance, with water. Valid background pixels having $\rho_{SWIR2} < 0.05$ and $\rho_{NIR} < 0.15$ and NDVI < 0 are considered to be water pixels. The number of such pixels is denoted as N_{uw}. If the absolute threshold test (Section 3.2.3) is not satisfied and $N_{uw}>0$, the tentative fire pixel is rejected and classified as a non-fire pixel, otherwise it is classified as an active fire pixel.

5 ASSUMPTIONS AND LIMITATIONS

Main Assumptions

- Unsaturated, spatially co-located data from all SLSTR channels required by the algorithm are available.
- Pixels containing cloud and water bodies have been masked out before the algorithms application, though pixels containing smoke remain unmasked.
- The SLSTR radiance measurements are well calibrated across the full range of spectral radiances measured over active fire pixels and background pixels.
- Duplicate pixels created during the data remapping process at level 1 will be identified as such so that duplicate fire pixels can be removed if desired.
- The area of the Earth (in m²) covered by each SLSTR pixel to be processed is available to the algorithm.
- An estimate of the atmospheric transmissivity in the SLSTR MIR channel is available to the algorithm, together with an estimate of the uncertainty in this value.
- The algorithm ignores the effects of increased aerosol and trace gas concentration above fires on the atmospheric transmissivity in the MIR channel (and indeed other channels).
- The fire and background emission are isotropic and approximate greybodies.

- The Planck's radiation law is well approximated by a fourth order power law in the wavelengths that the MIR channel of SLSTR is sensitive to.

- The pixel fire fraction can be neglected in the calculation of FRP.

- The fire pixel background radiance can be estimated from the radiance of the surrounding non-fire pixels.

Main Limitations

- The smallest/most weakly burning component of the fire regime will not be able to be detected with the moderate spatial resolution SLSTR instrument (fires covering down to perhaps 10^{-3} - 10^{-4} of a pixel will however be detectable).
- The FRP for a fire pixel may have some dependence on where the sub-pixel sized fire lies within the pixel area.
- The overpass time of the Sentinel-3 satellite is non-optimum for capturing the peak of the fire diurnal cycle (Figure 2).

6 INPUTS AND OUTPUTS

Inputs (at each SLSTR pixel)

- Cloud masked radiances and reflectances in the SLSTR Optical Channels (S1 to S6)
- Radiances and brightness temperatures in the SLSTR Thermal Channels (S7 to S9 & F1 and F2)
- Pixel coordinates (latitude/longitude)
- Water vapor fields
- Satellite zenith angles
- Solar zenith angles
- Ground pixel (km^2)
- Mask representing the land area potentially capable of supporting land based hotspots (i.e. the land surface with larger lakes and rivers masked out).
- Mask representing the location of industrial hotspots and volcanically active zones
- Mask representing the area of oceans and large lakes that might potentially be the sites of offshore gas flares.

Suggested Outputs

At each detected fire pixel

- Hotspot pixel coordinates (column/row and latitude/longitude)
- Hotspot date and time
- FRP (MW)
- FRP uncertainty (MW)
- Fire pixel confidence
- Hotspot class (land hotspot in industrial region, land hotspot in volcanic region, vegetation fire, oceanic hotspot, detected from F1, unknown, Not Processed due to S7 background saturation)
- Atmospheric transmittance
- Ground pixel area (km^2)
- Size of background window (b_w)
- Satellite zenith angle ( )

- MIR brightness temperature of fire pixel
- TIR brightness temperature of fire pixel
- Mean MIR brightness temperature of the valid background window pixels
- Mean TIR brightness temperature of the valid background window pixels

Raster mask covering the entire SLSTR scene classified into the following classes: cloudy land pixels; cloud free land pixels; cloudy water pixels; cloud free water pixels; confirmed fire pixels coded according to the hotspot class (land hotspot in industrial region, land hotspot in volcanic region, vegetation fire, oceanic hotspot, unknown). This raster mask can compress to a small size and be similar to that used in the MOD14 and MYD14 MODIS Fire Products (Giglio *et al.*, 2003).

7 Visual Examination and Evaluation

SLSTR-3A was launched on 16 Feb 2016. Soon after the pre-launch algorithm of Wooster *et al.*, (2012) was tested with real SLSTR data. Figure 13 shows an example application to SLSTR imagery collected at 05:15 UTC on 13 May 2016, when a large fire affected Fort McMurray, Alberta (Canada). Almost all the active fire pixels appear to be correctly identified in this case.

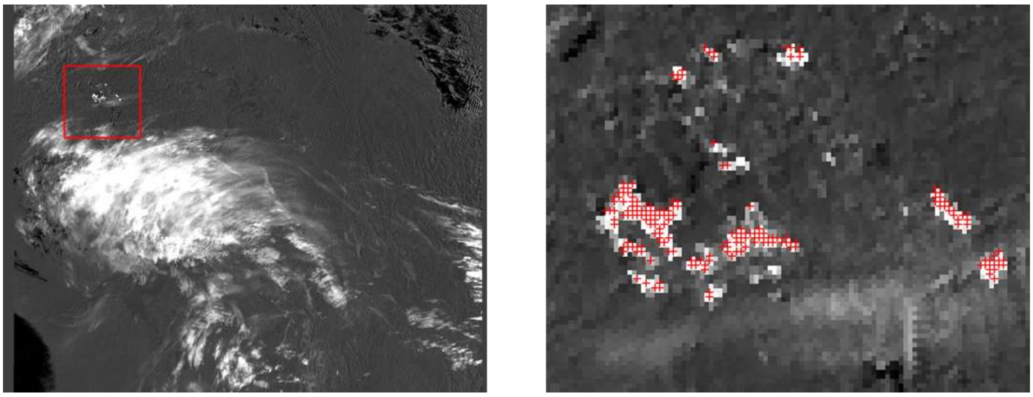

Figure 13. Example of the outputs of the SLSTR active fire detection process applied to night-time S3A data of the Fort McMurray fire in Alberta, Canada. Data were collected bySLSTR at 05:15 UTC on 13 May 2016. Background image is the MIR – TIR brightness temperature difference scene, with the zoom around the Fort McMurray region at right. Red crosses indicate the locations of detected active fire pixels.

In terms of oceanic hotspots, the following figures show examples of these detections.

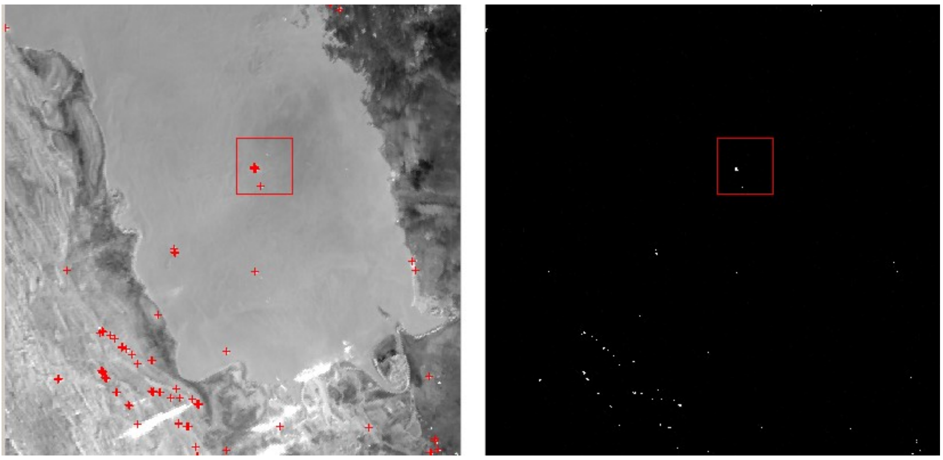

Figure 14. Example of oceanic gas flares detected at night in Iraq. Data is from a night-time S3A overpass at 18:48 UTC on 24 May 2016. Background image on the left is the MIR – TIR brightness temperature difference image, whilst that at right is the matching S6 spectral radiance image. Red crosses indicate locations of detected hotspot pixels.

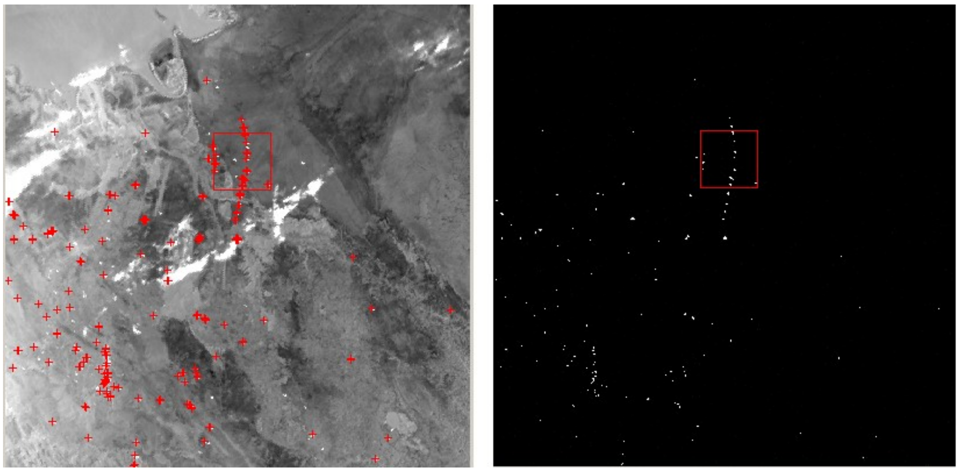

Figure 15. Further detection of gas flares, but this time onshore in Iraq. Same scene as in Fig. 10, but the location is further south. Background image on the left is the MIR – TIR brightness temperature difference image, whilst that at right is the matching S6 spectral radiance image. Red crosses indicates locations of detected hotspot pixels. S6 is very effective at detecting the gas flare locations.

8 REFERENCES

Arino, O., S. Plummer and S. Casadio (2007). Fire Disturbance: the Twelve years time series of the ATSR World Fire Atlas. Proceedings of the ENVISAT Symposium 2007, SP-636, ESA

Bond W.J. and van wilgen B.W. (1996). Fire and Plants. London: Chapman and Hall.

Casadio, S.; Arino, O.; Serpe, D (2012). Gas flaring monitoring from space using the ATSR instrument series. Remote Sens. Environ. 116, 239–249.

Csiszar, I. Arino, O., Geraci, R., Giglio, L., Goldammer, J., Justice, C., Kondragunta, S., Prins, E., Sessa, R., Tansey, K., and Wooster, M. (2008). Essential Climate Variable: Fire Disturbance, GTOS Report ECV T13 (http://www.fao.org/GTOS/ECV-T13.html)

Csiszar, I., Denis, L., Giglio, L., Justice, C.O., Hewson, J. (2005). Global fire activity from two years of MODIS data. International Journal of Wildland Fire, 14:117-130.

Dennison, P.E., K. Charoensiri, D.A. Roberts, S.H. Peterson, and R.O. Green (2006). Wildfire temperature and land cover modeling using hyperspectral data. Remote Sensing of Environment, 100, 212-222

Dozier, J. (1981). A method for satellite identification of surface temperature fields of subpixel resolution. Remote Sensing of Environment, 11:221-229.

Fisher, D.; Wooster, M.J. Shortwave IR Adaption of the Mid-Infrared Radiance Method of Fire Radiative Power (FRP) Retrieval for Assessing Industrial Gas Flaring Output. Remote Sensing 2018, 10, 305.

Flasse, S. P. and P. Ceccato a (1996). A contextual algorithm for AVHRR fire detection. International Journal of Remote Sensing, Volume 17, Issue 2 January 1996 , pages 419 - 424

Freeborn, P.H., Wooster, M.J., Hao, W.M., Ryan, C.A.,Nordgren, B.L. Baker, S.P. and Ichoku, C.(2008). Relationships between energy release, fuel mass loss, and trace gas and aerosol emissions during laboratory biomass fires, J. Geophys. Res., Vol. 113, No. D1, D01102, 10.1029/2007JD008489.

Freeborn, Patrick H., et al. "Quantification of MODIS fire radiative power (FRP) measurement uncertainty for use in satellite-based active fire characterization and biomass burning estimation." Geophysical Research Letters 41.6 (2014): 1988-1994.

Fuller Douglas O. (2000). Satellite remote sensing of biomass burning with optical and thermal sensors, Progress in physical geography, vol. 24, no4, pp. 543-561.

Gallegos, S., Ryan, R., Holekamp, K., Baud, R. and Bloemker, J. (2007) MODIS products to improve the monitoring of gas flaring from offshore oils and gas facilities, Final Report to NASA Science Mission Directorate, 10pp.

Generoso, S., Bréon, F.M, Balkanski, Y., Boucher, O. and Schulz, M.(2003). Improving the seasonal cycle and interannual variations of biomass burning aerosol sources, Atmos. Chem. Phys. 3, 1211-1222.

Giglio, L. (2005). MODIS Collection 4 Active Fire Product User's Guide Version 2.2, NASA [Online] Available: http://modis-fire.umd.edu/products.asp

Giglio, L. and J. D. Kendall (2001). Application of the Dozier retrieval to wildfire characterization—A sensitivity analysis. Remote Sens. Environ., vol. 77, 1226 no. 1, pp. 34–49.

Giglio, L. and Justice, C. (2003). Effect of wavelength selection on characterization of fire size and temperature, IJRS, 24, 3515-3520

Giglio, L. and Kendall, J. D. (2001). Application of the Dozier retrieval to wildfire characterization: A sensitivity analysis. Remote Sensing of Environment, 77:34-49.

Giglio, L. J. D. Kendall, and C. O. Justice (1999). Evaluation of global fire detection algorithms using simulated AVHRR infrared data. Int. J. Remote Sens., vol. 20, no. 10, pp. 1947–1985.

Giglio, L. J. D. Kendall, and R. Mack (2003a). A multi-year active fire dataset for the tropics derived from the TRMM VIRS. Int. J. Remote Sens., vol. 24, no. 22, pp. 4505–4525.

Giglio, L., Csiszar, I., Justice, C.O. (2006a). Global distribution and seasonality of active fires as observed with the Terra and Aqua MODIS sensors. Journal of Geophysical Research - Biogeosciences, Vol 111, doi:10.1029/2005JG000142

Giglio, L., J. Descloitres, C. O. Justice, and Y. J. Kaufman (2003b). An enhanced contextual fire detection algorithm for MODIS. Remote Sens. Environ., vol. 87, no. 2/3, pp. 273–282.

Giglio, L., van der Werf, G. R., Randerson, J. T., Collatz, G. J., and Kasibhatla, P. S. (2006b). Global estimation of burned area using MODIS active fire observations. Atmospheric Chemistry and Physics, 6:957-974.

Ichoku, C. and Y.J.Kaufman, L. Giglio, Z. Li, R.H. Fraser, J.Z.Jin, and W.M.Park, (2003). Comparative analysis of daytime fire detection algorithms using AVHRR data for the 1995 fire season in Canada: perspective for MODIS. Int.J. Remote Sensing, vol.24, no.8 pp. 1669-1690.

Ichoku, C., Kaufman, Y.J. (2005). A method to derive smoke emission rates from MODIS fire radiative energy measurements. Geoscience and Remote Sensing, IEEE Transactions on Volume 43, Issue 11, 2636 – 2649 DOI:10.1109/TGRS.2005.85732

Jordana, N.S., Charles Ichokub, C and Raymond M. Hoffa (2007). Estimating smoke emissions over the US Southern Great Plains using MODIS fire radiative power and aerosol observations. Atmospheric environment, Volume 42, Issue 9, March 2008, Pages 2007-2022

Justice, C. O., Giglio, L., Korontzi, S., Owens, J., Morisette, J. T., Roy, D., *et al.* (2002). The MODIS fire products. Remote Sensing of Environment, 83, 244–262.

Kaufman, Y.J. R.G. Kleidman and M.D. King (1998). SCAR-B fires in the tropics: properties and remote sensing from EOS-MODIS, Journal of Geophysical Research 103, pp. 31955–31968.

Kaufman, Y.J., Justice, C.O., Flynn, L.P., Kendall, J.D., Prins, E.M., Giglio, L., Ward, D.E., Menzel, W.P., and Setzer, A.W. (1998). Potential global fire monitoring from EOS-MODIS. Journal of Geophysical Research, 103:32,215-32,238.

Lavorel, S., Flannigan, M., Eric F. Lambin, Mary C. Scholes (2006). Vulnerability of land systems to fire: Interactions among humans, climate, the atmosphere, and ecosystems. Mitig Adapt Strat Glob Change, DOI 10.1007/s11027-006-9046-5

Levine, J. (1996). Biomass Burning and Global Change: Remote sensing, modeling and inventory development, and biomass burning in Africa, MIT Press, 1996, 551pp

Loboda, T. and Csiszar, I. (2007). Reconstruction of Fire Spread within Wildland Fire Events in Northern Eurasia from the MODIS Active Fire Product. Global and Planetary Change, 56 (3-4): 258-273 .

Roberts, G. and Wooster M.J. (2008). Fire detection and fire characterization over Africa using Meteosat SEVIRI. IEEE Transactions on Geoscience and Remote Sensing, 46, 1200-1218, doi: 10.1109TGRS.2008.915751

Roberts, G., Wooster, M.J., Perry, G.L.W., Drake, N., Rebelo, L-M., Dipotso, F. (2005). Retrieval of biomass combustion rates and totals from fire radiative power observations: Application to southern Africa using geostationary SEVIRI Imagery. Journal of Geophysical Research, 110, D21111, doi: 10.1029/2005JD006018

Robinson, J.M. (1991). Fire from the space: Global fire evaluation using infrared remote sensing. Int. J. Remote sensing, vol.12, no.1 pp. 3-24.

Schaaf, C. (2008). Albedo and Reflectance Anisotropy, Terrestrial Essential Climate Variables for Climate Change Assessment, Mitigation and Adaptation. GTOS-52, Eds. R. Sessa and H. Dolman, FAO, Rome, 28-29.

Schultz, M. (2002). On the use of ATSR fire count data to estimate the seasonal and interannual variability of vegetation fire emissions. Atmos. Chem.Phys., vol. 2, no. 5, pp. 387–395.

Sinha, P., Jaeglé, L., Hobbs, P.V. and Q. Liang (2004). Transport of biomass burning emissions from southern Africa, . J. Geophys. Res., 109, D20204, doi:10.1029/2004JD005044.

Sukhinin, A. I. Nancy H.F. French,, Eric S. Kasischke, Jenny H. Hewson, Amber J. Soja, Ivan A. Csiszar, Edward J. Hyer, Tatiana Loboda, Susan G. Conrad, Victor I. Romasko, Eugene A. Pavlichenko, Sergey I. Miskiv and Olga A. Slinkina (2004). AVHRR-based mapping of fires in Russia: New products for fire management and carbon cycle studies, Volume 93, Issue 4, Pages 546-564

Sullivan, A. L., P. F. Ellis and I. K. Knight (2003). A review of radiant heat flux models used in bushfire applications, international Journal of Wildland Fire. 12(1) 101 – 110

Thompson, A.M., Witte, J.C, Hudson,R.D., Guo, H., Herman, J.R., Fujiwara, M. (2001). Tropical Tropospheric Ozone and Biomass Burning. Science, 291, 16.

Van der Werf, G.R., J.T. Randerson, L. Giglio, G.J. Collatz, P.S. Kasibhatla (2006). Interannual variability in global biomass burning emissions from 1997 to 2004. Atmos. Chem. Phys. Discuss., 6, 3175-3226.

Wooster, M.J. and Rothery, D.A. (1997) Thermal monitoring of Lascar Volcano, Chile, using infrared data from the along-track scanning radiometer: a 1992–1995 time series. Bulletin of Volcanology, 58(7), pp.566-579.

Wooster, M.J. and Strub, N. (2002). Study of the 1997 Borneo Fires: Quantitative analysis using Global Area Coverage GAC. satellite data, Global Biogeochemical Cycles 161: doi:10.1029/2000GB001357

Wooster, M.J., B. Zhukov, and D. Oertel (2003). Fire radiative energy for quantitative study of biomass burning: Derivation from the BIRD experimental satellite and comparison to MODIS fire products, Remote Sens. Environ., 1410 vol. 86, no. 1, pp. 83–107.

Wooster, M.J., G. Roberts, G. L. W. Perry, and Y. J. Kaufman (2005). Retrieval of biomass combustion rates and totals from fire radiative power obser vations: FRP derivation and calibration relationships between biomass consumption and fire radiative energy release. J. Geophys. Res., vol. 110, no. D24, p. D24 311, DOI:10.1029/2005JD006318.

Wooster, M.J., Zhukov, B. and Oertel, D. (2003). Fire radiative energy for quantitative study of biomass burning: Derivation from the BIRD experimental satellite and comparison to MODIS fire products. Remote Sensing of Environment 86: 83-107.

Wooster, M.J., Xu, W. and Nightingale, T. (2012). Sentinel-3 SLSTR active fire detection and FRP product: Pre-launch algorithm development and performance evaluation using MODIS and ASTER datasets. Remote Sensing of Environment, 120, 236-254.

Xie, Y., Qu, J.J., Hao, W., Che, N., and Sommers, E. (2007). Smoke plume detection in the eastern United States using MODIS. International Journal of Remote Sensing, 28, 2367-2374

Zhukov, B., Lorenz, E., Oertel, D., WOOSTER, M.J. and Roberts, G. (2006). Space borne detection and characterization of fires during the Bi-spectral Infrared Detection (BIRD) experimental small satellite mission 2001-2004. Remote Sensing of Environment 100: 29-51.

Tabel A.1 Look up table of atmosphere correction parameters

UH_2O	τ	A	B	C
5	0.132334	0.03464	0.807271	0.109722
10	0.167676	0.034524	0.797931	0.109198
15	0.198686	0.035494	0.783314	0.113246
20	0.226906	0.036565	0.769342	0.118173
25	0.253197	0.037469	0.757317	0.12285
30	0.278131	0.038189	0.7473	0.126978
35	0.305502	0.0387	0.740741	0.130468
40	0.333303	0.039033	0.736158	0.133339
45	0.361108	0.039229	0.732941	0.135641
50	0.384307	0.039393	0.728737	0.137681
55	0.408425	0.03947	0.725873	0.139317
60	0.429562	0.039525	0.722495	0.140805